The Planetary Science Journal, 7:22 (19pp), 2026 January https://doi.org/10.3847/PSJ/ae1fda
© 2026. The Author(s). Published by the American Astronomical Society.
OPEN ACCESS

The Effect of Colored Noise on Doppler Measurements for Planetary Geodesy: Application to the VERITAS Gravity Science Experiment

Flavia Giuliani[1], Fabrizio De Marchi[1], Daniele Durante[1], Gael Cascioli[2,3], Luciano Iess[1], Erwan Mazarico[3], and Suzanne Smrekar[4]
[1] Department of Mechanical and Aerospace Engineering, Sapienza University of Rome, 00184 Rome, Italy; flavia.giuliani@uniroma1.it
[2] University of Maryland, Baltimore County, MD 21250, USA
[3] NASA Goddard Space Flight Center, Greenbelt, MD 20771, USA
[4] NASA Jet Propulsion Laboratory, Pasadena, CA 91109, USA
Received 2025 August 6; revised 2025 November 12; accepted 2025 November 12; published 2026 January 26

Abstract

Measurements of the Doppler shift of a carrier signal have always been the basis of radio science experiments, particularly for planetary gravity field recovery. Doppler observables are affected by correlated (colored) noise; however, standard orbit estimation filters assume that the noise is white and Gaussian. This assumption simplifies the code and reduces the runtime, as the weight matrix is diagonal. In this work, we present a method for incorporating colored noise into least-squares estimation filters by constructing a full noise covariance matrix that reflects the spectral characteristics of all contributing error sources, guaranteeing the proper estimation of parameters and their associated uncertainties. We apply this methodology to the gravity science experiment of NASA's upcoming Venus Emissivity, Radio Science, InSAR, Topography, And Spectroscopy (VERITAS) mission. Our analysis finds that the white noise assumption is valid for VERITAS—thus supporting the robustness of earlier simulation results. The approach, however, is general and particularly valuable for future missions in which colored noise, such as plasma-induced red noise, dominates the Doppler error budget.

Unified Astronomy Thesaurus concepts: Gravitational fields (667); Venus (1763); Solar system terrestrial planets (797); Orbit determination (1175); Planetary science (1255)

1. Introduction

Radio science investigations for planetary gravity field studies rely almost entirely on accurate Doppler (range-rate) and, to a lesser extent, range observables, obtained by establishing a radio link between the spacecraft and a ground station. These observables are used to reconstruct the spacecraft's orbit and to estimate the key geophysical parameters of interest. To achieve an accurate estimation, it is essential to have a high-quality radio tracking system capable of providing high phase stability and ranging accuracy. Additionally, both the forces acting on the spacecraft and the noise affecting the radio link must be accurately modeled and considered.

With regard to the data noise—particularly the Doppler measurements, which are the focus of this work—it is nearly universal to assume an additive white Gaussian noise, characterized by uncorrelated samples in time and a flat power spectral density (PSD). This assumption has been adopted in the analysis of a large number of radio science experiments in planetary exploration missions (R. A. Mackenzie et al. 2008; A. Genova et al. 2016; D. Durante et al. 2020; A. S. Konopliv et al. 2020) and is generally valid when plasma and propagation effects are small (R. Mackenzie & W. M. Folkner 2006; D. R. Jones et al. 2016). Most orbit determination codes use a sequential or batch filter approach based on this assumption (G. J. Bierman 1977; T. D. Moyer 2003; J. C. Marty et al. 2011; S. Evans et al. 2018). However, real tracking data often exhibit correlated noise, leading to frequency-dependent PSDs, particularly under strong plasma conditions since plasma noise behaves as a red noise process (R. Mackenzie & W. M. Folkner 2006; D. R. Jones et al. 2016). Ignoring these correlations can lead to incorrect estimation of both the parameters of interest and their associated uncertainties (R. Mackenzie & W. M. Folkner 2006). The state-of-the-art literature shows two main approaches to handling strongly colored noise, typically associated with plasma noise: deweighting the Doppler data (R. A. Jacobson 2014, 2022; Opportunity data in P. Kuchynka et al. 2014) or applying a Doppler prewhitening algorithm (L. Iess et al. 2010; R. A. Jacobson 2014, 2022 only for close-encounter dataset; P. Kuchynka et al. 2014 for the data of Viking and Pathfinder landers; R. Mackenzie & W. M. Folkner 2006; R. S. Park et al. 2024). However, detailed descriptions of the prewhitening algorithm are limited in the public literature: some implementations are available only in internal documentation (R. Mackenzie & W. M. Folkner 2006), while others provide only partial outlines (P. Kuchynka et al. 2014) but do not constitute a complete, reproducible framework.

The primary objective of this work is therefore to develop a method for processing correlated noise measurements within a filtering framework that typically assumes white (uncorrelated) observations. Correlated noise is also called colored noise in analogy with the color spectrum, where spectral power depends on frequency. To achieve this, a whitening procedure is applied to the data prior to analysis, with the aim of flattening the PSD, decorrelating the measurements, normalizing the residuals, and thus obtaining a truthful estimate of the formal covariance matrix.

In this work, all datasets of colored noise have been generated by using the algorithm described in J. Timmer & M. Konig (1995; hereafter "TK"). For the calculus of the covariance matrices and for the whitening process, we developed a discrete procedure based on truncated series,

Original content from this work may be used under the terms of the Creative Commons Attribution 4.0 licence. Any further distribution of this work must maintain attribution to the author(s) and the title of the work, journal citation and DOI.

rather than on continuous domain integrals, showing that this approach is the most suitable to handle this kind of noise data. A recap of the TK method and a generalization to arbitrary PSDs (not power laws only) together with the formulae for the autocovariance functions have been reported in Appendix A.

Section 2 presents a detailed Doppler noise model, focusing on the different sources of noise and their spectral characteristics. Section 3 introduces the differences between white and colored noise and the approach adopted to simulate observables in both cases. Section 4 describes the whitening procedure in detail.

In this work we apply this methodology to the case of NASA's Venus Emissivity, Radio Science, InSAR, Topography, And Spectroscopy (VERITAS) mission to Venus, with the aim of validating and extending previous simulations of its onboard gravity science experiment, which were carried out under the assumption of white noise (F. Giuliani et al. 2025). VERITAS, a Discovery-class mission selected by NASA in 2021, is designed to address fundamental questions about Venus's geological activity and evolution, internal structure, and possible evidence of past or present interior water (S. Smrekar et al. 2022). Section 5 presents the VERITAS gravity science experiment simulations, detailing the dynamical model, noise sources, and estimation filter setup. Results are discussed in Section 6, where the implications of using colored versus whitened noise are evaluated in the context of gravity field recovery and geophysical parameter estimation.

2. Doppler Error Sources

The spacecraft range rate (often indicated as the line-of-sight velocity) can be inferred by observing the Doppler shift of a radio signal transmitted from an Earth station to the spacecraft, which then, maintaining phase coherence, retransmits it back to ground.

Doppler measurements are affected by noise originating from a variety of sources, which can be broadly classified into three main categories: propagation noise, electronic noise, and mechanical noise (S. W. Asmar et al. 2005; L. Iess et al. 2014). Propagation noise arises from phase and frequency shifts induced as the signal propagates through media, such as Earth's troposphere, Earth's ionosphere, and the interplanetary plasma. Electronic noise includes frequency shifts introduced by ground and spacecraft electronics and by the master frequency standards used in the generation and down-conversion of the carrier. Mechanical noise mainly results from wind loading, gravitational loading, and thermal expansion of the ground antenna and spacecraft buffeting and thermomechanical deformations.

Each noise source can be characterized either in the time domain or in the frequency domain. In the time domain, a widely used figure of merit in radio science investigations for characterizing Doppler measurement noise is the Allan deviation (ADEV; F. L. Walls & D. W. Allan 1986), denoted by $\sigma_y(\tau)$, which quantifies the frequency stability over a duration τ.

We define the time-error function $x(t)$ as the difference between the time of the clock and a reference time. Its PSD, $S_x(f)$, represents the distribution of the power among various frequencies f. We also define

$$y(t) = \frac{dx}{dt} \tag{1}$$

and the corresponding PSD,

$$S_y(f) = (2\pi f)^2 S_x(f). \tag{2}$$

Finally, we define the estimator,

$$y_1(t, \tau) = \frac{x(t+\tau) - x(t)}{\tau}, \tag{3}$$

which represents the Doppler data (where τ is the integration time).

The Allan Variance (AVAR) is, by definition, the variance of the estimator

$$y_2(t, \tau) = \frac{y_1(t+\tau) - y_1(t)}{\sqrt{2}}. \tag{4}$$

It can be demonstrated that (F. L. Walls & D. W. Allan 1986)

$$\sigma_y^2(\tau) = 2\int_0^{+\infty} S_y(f) \frac{\sin^4(\pi f\tau)}{(\pi f\tau)^2} df. \tag{5}$$

For our purposes, we model the PSDs by power laws (we adopt the one-sided spectrum convention). In particular,

$$S_x(f) = h_x f^{\beta}; S_y(f) = h_y f^{\alpha}; h_y = 4\pi^2 h_x; \beta = \alpha - 2, \tag{6}$$

where h_x and h_y are noise intensity coefficients and α and β are the power-law exponents that determine the slopes of the PSDs on a log–log plot.

Different types of colored noise correspond to different values of α (e.g., white frequency noise corresponds to $\alpha = 0$, while white phase noise corresponds to $\alpha = 2$).

In the following sections, the main Doppler noise sources are briefly described, with a focus on the characteristic noise color of each, defined by the slope α. Particular attention is given to plasma (Section 2.1) and tropospheric (Section 2.2) noise, due to their nonstationary behavior, which complicates their modeling.

In the subsequent analysis, knowing the expected AVARs and the colors of the noise sources, we will obtain the corresponding numerical coefficients h_y necessary to generate noise datasets with the required properties. To this aim, we refer the reader to Appendix A, where we describe the details of the simulation of colored noise and the calculus of the expected covariance function.

2.1. Plasma

One of the most significant noise sources in spacecraft tracking systems is related to the effect of charged particles, primarily from interplanetary and coronal plasma, as well as from the ionosphere, the latter of which can be modeled more accurately via ground-based GNSS measurements. Plasma noise is one of the most complex contributions to model because of its dependence on the solar cycle and the unpredictable nature of solar activity, which makes accurate modeling particularly challenging.

L. Iess et al. (1983) developed a model for the Doppler noise that results from discontinuities and MHD waves of the interplanetary plasma. The model is based on the "frozen-in" hypothesis, whereby the density fluctuations of the plasma are static structures that are carried by the solar wind.

In agreement with the frozen-in hypothesis, the spectrum of the plasma density fluctuations for a signal propagating between points n and f can be expressed as the combination

Table 1
Plasma Doppler Noise ADEV Parameters

Symbol	Physical Quantity	Numerical Value
ϵ_0	Vacuum permittivity	8.854×10^{-12} F m^{-1}
c	Speed of light	3.00×10^{8} m s^{-1}
m_e	Electron mass	9.109×10^{-31} kg
V_0	Solar wind speed	400 km s^{-1}
L_D	Discontinuity scale length	2×10^{6} km
r_0	Reference heliocentric distance	1 au
q	Numerical coefficient	4.16
$<\delta n^2>$	Quadratic mean electron density	3.766×10^{12} m^{-6}
p_D	Kolmogorov coefficient	$\frac{11}{3}$

of two effects: the fluctuations of the refraction index over the scale of the solar system (i.e., astronomical units) and on the turbulence scale (i.e., $\approx 10^6$ km).

The contribution to radio fluctuations due to discontinuities is proportional to the component of the solar wind velocity perpendicular to the line of sight (hence the Sun–probe–Earth (SPE) angle), say, $V_\perp$, and becomes especially significant near superior solar conjunctions.

The other component, due to MHD waves, can be separated from the first one only near inferior conjunctions (or solar oppositions, for a spacecraft in the outer solar system) when the noise due to discontinuities vanishes. Since at inferior conjunctions the Doppler noise is dominated by other sources, we will consider only the component due to discontinuities.

We report here the basic elements of the model; for more details see L. Iess et al. (1983).

Consider two points, n (near) and f (far) at heliocentric distances r_n and r_f, where $r_n < r_f$, respectively. The angle θ represents the Sun–n–f angle. Consider a point P on the n-to-f line of sight and call η the n-to-P distance. The Sun-to-P distance is

$$r(\eta) = \left(r_n^2 - 2\eta r_n \cos\theta + \eta^2\right)^{1/2}, \tag{7}$$

the n-to-f distance is

$$L(\theta) = r_n\left[\cos\theta + \sqrt{\left(\frac{r_f}{r_n}\right)^2 - \sin^2\theta}\right] \tag{8}$$

and

$$V_\perp = V_0 \sin\theta\left[1 - 2\frac{\eta}{r_n}\cos\theta + \frac{\eta^2}{r_n^2}\right]^{-1/2} \tag{9}$$

We assume that the refraction index fluctuations over the solar system scale follow a power-law profile

$$g(\eta) = \left(\frac{r_0}{r}\right)^q = \left(\frac{r_0}{r_n}\right)^q\left[1 - 2\frac{\eta}{r_n}\cos\theta + \frac{\eta^2}{r_n^2}\right]^{-q/2}, \tag{10}$$

where q is a numerical coefficient expected to be between 4 and 5 (L. Iess et al. 1983).

Over the short scale we adopt a Kolmogorov spectrum (κ is the wavenumber),

$$W_D = \frac{1}{\left(1 + L_D^2\kappa^2\right)^{p_D/2}}, \tag{11}$$

where $p_D = 11/3$ and L_D is the scale length of the discontinuities (we will assume $L_D = 2 \times 10^6$ km). With these assumptions, the PSD of the Doppler noise due to plasma discontinuities is ($\omega = 2\pi f$)

$$S_{y,\mathrm{plasma}}(\omega, \theta) \propto \langle\delta n^2\rangle \int_0^{L(\theta)} d\eta g(\eta) \times \int_{\omega/V_\perp}^{+\infty} \kappa d\kappa W_D(\kappa)\left[(\kappa V_\perp)^2 - \omega^2\right]^{-1/2}, \tag{12}$$

where $\langle\delta n^2\rangle$ is the quadratic mean electron density at a distance r_0 from the Sun and the symbol "$\propto$" encompasses normalizing factors (for more details see L. Iess et al. 1983).

The discontinuities crossing the line of sight produce fluctuations at a frequency of the order of $V_0/L_D \approx 0.2$ mHz or less, quite below the range of our interest.

In the hypothesis $2\pi f L_D \gg V_\perp$, the PSD of the plasma is well represented by a power-law profile

$$S_{y,\mathrm{plasma}} = h_{y,\mathrm{pl.}} f^{\alpha_{\mathrm{pl.}}}, \tag{13}$$

where the spectral index α is given by

$$\alpha_{\mathrm{pl.}} = 3 - p_D. \tag{14}$$

This implies $S_{y,\mathrm{plasma}}(f) \propto f^{-\frac{2}{3}}$ (i.e., a "red" noise).

Applying Equations (5)–(13) and taking into account the normalizing factors, the Allan variance for plasma noise can be expressed as

$$\sigma^2_{\mathrm{plasma}}(\tau, \theta) = w(1 - P_{\mathrm{calib}})^2\tau^{p_D-4}\frac{<\delta n^2>}{\nu_0^4} \frac{e^4\left(1 - 2^{p_D-4}\right)\Gamma(2 - p_D)}{16\pi^5 c^2\epsilon_0^2 m_e^2}(p_D - 3)\cos\left(\frac{\pi p_D}{2}\right) L_D^{3-p_D}\left(\frac{r_0}{r_n}\right)^q (V_0 \sin\theta)^{p_D-2} I(\theta), \tag{15}$$

where

$$I(\theta) = \int_0^{L(\theta)}\left[1 - \frac{2\eta}{r_n}\cos\theta + \left(\frac{\eta}{r_n}\right)^2\right]^{1-\frac{q+p_D}{2}} d\eta. \tag{16}$$

For the VERITAS mission, to which the methodology is first applied, object n corresponds to Venus and f to Earth. Thus, in this context, θ is the SPE angle. The carrier frequency ν_0 and integration time τ are parameters related to the specific radio science experiment. For VERITAS, $\nu_0 = 34.384$ GHz (Ka-band link), and an optimal sampling time is $\tau = 10$ s (F. Giuliani et al. 2025).

The numerical values of the parameters q and $<\delta n^2>$ have been obtained by fitting the model to BepiColombo and Cassini Doppler noise data. Details about the calibration of the model will be published in an upcoming paper (F. De Marchi et al., in preparation). Table 1 reports the physical constants and parameters used in Equation (15).

The factor w equals 1 for a one-way Doppler system and 2 for a two-way link (i.e., both uplink and downlink), as plasma noise affects both legs. To compute the intensity coefficient $h_{y,\mathrm{pl.}}$, Equation (15) can be used once $\sigma^2_{\mathrm{plasma}}$ is known.

As shown by Equation (15), an increase in the carrier frequency leads to a significant reduction in plasma noise. For example, the use of Ka-band can significantly mitigate the noise with respect to an X-band link. Additionally, plasma noise can be fully or partially calibrated using a multifrequency radio link

(B. Bertotti et al. 1993; G. Mariotti & P. Tortora 2013). The factor P_{calib} in Equation (15) quantifies the percentage of calibration applied.

2.2. Troposphere

Tropospheric noise originates from variations in the refractive index encountered by the signal as it travels through Earth's troposphere, resulting in propagation delays. This noise can be attributed to two main sources: a dry component, which is dominant (∼90% of the total tropospheric delay) but can be accurately modeled to within a few millimeters of zenithal path delay under common meteorological conditions (C. L. Thornton & J. S. Border 2003), and a wet component, which arises from fluctuations in the atmospheric water vapor content (D. R. Buccino et al. 2021). Although the wet component is typically smaller in magnitude, it is less stable in time (wet-delay fluctuation levels are approximately three times those of the dry component; S. J. Keihm et al. 2004) and thus more difficult to predict and correct. The noise intensity is time dependent; more specifically, the wet troposphere water vapor content exhibits seasonal variability. In the Northern Hemisphere, it tends to be lower during winter nights and higher during summer days; the opposite trend is observed in the Southern Hemisphere (L. Iess et al. 2014).

In the frequency domain, tropospheric noise can be assumed to be white (see Appendix B): $S_{y,\text{tr}}(f) = h_{y,\text{tr}}(t)f^0$. From Equation (A.8) with $\alpha = 0$ and integrating in the domain $z \in [0, +\infty[$, we find

$$\sigma^2_{y,\text{tr}}(t) = \frac{h_{y,\text{tr}}(t)}{2\tau}. \tag{17}$$

For all these reasons, following L. Iess et al. (2014), we modeled the ADEV of the wet troposphere with a sinusoidal trend having annual periodicity. We express the AVAR as

$$\sigma^2_{y,\text{tr}}(t) = w * \left(\frac{\tau_0}{\tau}\right) * (1 - T_{\text{calib}})^2 * \left(\frac{\sigma_s + \sigma_w}{2} + s_{\text{hemisphere}} * \frac{\sigma_s - \sigma_w}{2} \cos\left(\frac{2\pi}{T}(t - t_{\text{solstice}})\right)\right)^2. \tag{18}$$

Here $\sigma_s = 7.56632 \times 10^{-14}$ and $\sigma_w = 1.60744 \times 10^{-14}$ are parameters derived from L. Iess et al. (2014), representing the uncalibrated ADEV at summer and winter solstice, referred to an integration time $\tau_0 = 100$ s. The time T corresponds to 1 yr, representing the period of the seasonal modulation, while t_{solstice} indicates the epoch of a local summer solstice. The sign factor $s_{\text{hemisphere}}$ is equal to +1 for the Northern Hemisphere and −1 for the Southern Hemisphere, to account for the opposite seasonal behavior. As with plasma noise, the coefficient $w = 1$ or 2 is used to distinguish between one-way and two-way Doppler tracking configurations, respectively. The term T_{calib} accounts for the percentage of noise reduction achievable through calibration using water vapor radiometers, which can significantly mitigate the wet tropospheric contribution (D. R. Buccino et al. 2021).

2.3. Other Noise Sources

In addition to solar plasma and tropospheric contributions, the ionosphere also affects the Doppler signal. As the radio link propagates through the ionosphere, interactions with charged particles introduce additional Doppler shifts. Similarly to interplanetary plasma effects, ionospheric noise can be calibrated using a multifrequency radio link.

Several onboard sources contribute to the overall Doppler noise budget. These include elements of the radio frequency subsystem such as the transponder and the traveling wave tube amplifier (TWTA), both of which exhibit thermal (i.e., $\alpha = +2$) and white noise characteristics. Additionally, spacecraft buffeting introduces further Doppler fluctuations, typically modeled as a white noise.

On the ground segment, Doppler noise is generated from various components of the tracking infrastructure. The frequency and timing system (FTS) can be modeled with several white, thermal, and red (i.e., $\alpha < 0$) components. The receiver chain introduces white and thermal noise, while the transmitter chain and mechanical disturbances of the ground station antenna can be modeled as white noise (L. Iess et al. 2014).

Table 2 summarizes the Doppler noise sources considered in this study, indicating their dependence on the integration time τ in terms of Allan deviation. Each noise contribution is also categorized according to its spectral color: white, red, or thermal. As shown in the table, some sources exhibit different slopes over different integration time intervals, which correspond to changes in their spectral behavior (and thus their spectral color). To simplify the analysis without introducing significant error, instead of using a piecewise function, we assume the different spectral behaviors for each source to be valid across the entire τ range considered, and we compute the total noise for each color as the quadratic sum of the contributions from the individual sources assigned to that color.

In the case of thermal noise (i.e., $\alpha = +2$), to obtain the ADEV, Equation (5) cannot be used, as the integral diverges.

Table 2
Summary of Doppler Noise Sources, Their Allan Deviation Dependence on Integration Time τ, and Corresponding Noise Classification

Noise Sources	ADEV Dependence on τ		Noise Type
Plasma (two-way)	$\tau^{-\frac{1}{6}}$	…	Red
Troposphere (two-way)	$\tau^{-\frac{1}{2}}$	…	White
Ionosphere (two-way)	$\tau^{-\frac{1}{2}}$	…	White
Frequency and timing system (FTS; one-way)	τ^{-1}	$\tau < 20$ s	Thermal
	$\tau^{-\frac{1}{2}}$	20 s $< \tau <$ 1000 s	White
	$\tau^{0.27}$	$\tau >$ 1000 s	Red
Receiver chain (Rx; one-way)	τ^{-1}	$\tau <$ 100 s	Thermal
	$\tau^{-\frac{1}{2}}$	$\tau >$ 100 s	White
Transmitter chain (Tx; one-way)	$\tau^{-\frac{1}{2}}$	…	White
Ground station antenna (GS; two-way)	$\tau^{-\frac{1}{2}}$	…	White
Spacecraft buffeting (two-way)	$\tau^{-\frac{1}{2}}$	…	White
Integrated deep space transponder (IDST; one-way)	τ^{-1}	$\tau <$ 1000 s	Thermal
	$\tau^{-\frac{1}{2}}$	$\tau >$ 1000 s	White
Traveling wave tube amplifier (TWTA; one-way)	τ^{-1}	…	Thermal
	$\tau^{-\frac{1}{2}}$	…	White
Spacecraft high-gain antenna (HGA; two-way)	$\tau^{-\frac{1}{2}}$	…	White

By using Equation (A.8) (or Equation (A.29) in the limit of large N), one finds ADEV $\propto\tau^{-1}$.

It is important to notice again that the classification of noise type (e.g., white, red, thermal) is based on their spectral behavior (the coefficient α in Equation (6)), not on the slope of their Allan deviation across time (the corresponding Allan variance is, for $-3 < \alpha < +1$, proportional to $\tau^{-\alpha-1}$; see Appendix A).

3. Simulation of Colored Noise

White Doppler noise is characterized by a flat PSD, meaning that its power is uniformly distributed across all frequencies. Consequently, its autocorrelation function (ACF), defined as the autocovariance function normalized by the variance (i.e., $R_y(\tau)/R_y(0)$), is zero at all nonzero lags and equal to unity at lag zero. This implies that the measurements are uncorrelated, and the associated noise covariance matrix R ($R = E[\epsilon\epsilon^T]$; see Appendix A for further details) is diagonal.

However, real Doppler tracking data will typically exhibit colored noise. In a log–log plot, the PSD appears as a nonzero slope, directly linked to the spectral color of the noise (see Section 6.1, in which residuals, PSDs, and ACFs for a test pass of VERITAS are reported). The time correlation of the noise results in nonzero off-diagonal elements in the noise covariance matrix.

For simulations involving only white noise, synthetic Doppler observables can be generated by adding random noise drawn from a Gaussian distribution with zero mean and a standard deviation given by the quadratic sum of the Allan deviations of each contributing noise source at the appropriate integration time. In contrast, simulating colored noise requires a different approach. We used the TK algorithm to generate synthetic stochastic time series with a specified power law (see Appendix A.1).

4. Orbit Determination with Colored Noise

Most orbit determination codes, such as MONTE, GEODYN, and GINS (J. C. Marty et al. 2011; S. Evans et al. 2018; Nicholas et al. 2025), adopt a filtering approach in which measurements are assumed to be uncorrelated. Consequently, the observation noise covariance matrix R is treated as diagonal. However, when the noise is colored, this assumption no longer holds: the measurements are time correlated, and R is a full matrix.

Generally, there are two ways to address this issue: either modify the software to directly account for correlations by including off-diagonal terms in the noise covariance matrix (P. Kuchynka et al. 2014), or preprocess the data to remove correlations before filtering. If neither method is applied, the resulting state vector and corresponding formal uncertainty will not provide an unbiased, minimum variance estimate. The first option is not supported by most OD codes, including MONTE and the proprietary filter used for these simulations (see Section 5.3 for details on the filter), which is designed to process measurement files from MONTE and therefore accounts only for a diagonal noise covariance matrix. For this reason, in this work we adopted the second approach: to consistently process the observations with the diagonal weight assumption, they are properly whitened before filtering.

Following the methodology presented in B. D. Tapley et al. (2004), the whitening procedure is detailed below, with emphasis on the computation of the noise covariance matrix in Section 4.1.

Given a set of observations, the linearized observation equation can be written as

$$y - Hx = \epsilon, \tag{19}$$

where y denotes the observed residuals, H is the mapping matrix containing the partial derivatives of the observations with respect to the state vector, x is the deviation state vector, and ϵ is the observation noise vector. The noise is assumed to be Gaussian with zero mean, $E[\epsilon] = 0$, and characterized by a covariance matrix $R = E[\epsilon\epsilon^T]$, which is symmetric and positive definite but not necessarily diagonal, with the off-diagonal terms capturing the temporal correlations of the noise.

The minimum variance, least-squares estimate of the state vector at a reference epoch is given by

$$\hat{x}_0 = \left(H^T R^{-1} H + \bar{P}_0^{-1}\right)^{-1}\left(H^T R^{-1} y + \bar{P}_0^{-1}\bar{x}_0\right), \tag{20}$$

where $\bar{P}_0$ and $\bar{x}_0$ are the a priori covariance matrix and state vector.

To whiten the observations, we apply a Cholesky decomposition to R, obtaining a lower triangular matrix V such that

$$R = VV^T. \tag{21}$$

Left-multiplying Equation (19) by V^{-1} gives

$$V^{-1}y - V^{-1}Hx = V^{-1}\epsilon. \tag{22}$$

Introducing the transformed variables,

$$\tilde{y} = V^{-1}y \tag{23}$$

$$\tilde{H} = V^{-1}H \tag{24}$$

$$\tilde{\epsilon} = V^{-1}\epsilon, \tag{25}$$

we obtain the whitened observation equation:

$$\tilde{y} - \tilde{H}x = \tilde{\epsilon}. \tag{26}$$

By construction, the transformed noise vector $\tilde{\epsilon}$ has zero mean and identity covariance, since

$$E[\tilde{\epsilon}] = V^{-1}E[\epsilon] = 0 \tag{27}$$

$$E\left[\tilde{\epsilon}\tilde{\epsilon}^T\right] = V^{-1}E[\epsilon\epsilon^T]V^{-T} = V^{-1}RV^{-T} = I. \tag{28}$$

This transformation enables the orbit determination filter to proceed using $\tilde{y}$ and treating the noise as white (uncorrelated), with the identity matrix as its covariance. In this case, the solution simplifies to

$$\hat{x}_0 = \left(\tilde{H}^T\tilde{H} + \bar{P}_0^{-1}\right)^{-1}\left(\tilde{H}^T\tilde{y} + \bar{P}_0^{-1}\bar{x}_0\right), \tag{29}$$

which is mathematically equivalent to the original expression in Equation (20). Consequently, the parameter covariance derived after whitening is identical to that obtained using the full colored noise covariance R. This equivalence formally validates that the whitening procedure correctly propagates the colored noise properties into the parameter estimation.

A key challenge in this approach is the computation of the noise covariance matrix R.

4.1. The Noise Covariance Matrix

Given the theoretical PSD $S_y(f)$ associated with each noise source, in Appendix A we report the procedure to generate a Doppler noise dataset (N even data, uniformly spaced by Δt and with integration time τ, the duration of the signal being $T = (N-1)\Delta t$).

The corresponding "expected" autocovariance function is given, in the most general case, by Equation (A.25), while Equation (A.26) corresponds to a power-law model. For simplicity, we put into Equation (A.26) $\Delta t = \tau$. By setting $h_y = 1$, we obtain

$$\bar{R}_{y,1}((j-1)\tau, \tau) = \frac{1}{N\pi^2\tau^3}\sum_{s=2}^{\frac{N}{2}} \nu_s^{\alpha-2} \sin^2\left(\frac{\pi(s-1)}{N}\right) \cos\left(2\frac{\pi(s-1)(j-1)}{N}\right) j = 1,\ldots,\frac{N}{2}+1. \quad (30)$$

In this expression, ν_s is a vector of $N/2$ equally spaced frequencies between $1/T$ and the Nyquist frequency (see Equation (A.14)); N is the number of uniformly spaced data points in the simulated Doppler noise series, each separated by a sampling interval $\Delta t = \tau$; and j is the index corresponding to the ratio between the sample time and the integration time $\left(i.e., j = \frac{t}{\tau}\right)$. This equation provides the expected discrete autocovariance function of a Doppler noise process characterized by a power-law PSD. Derived from the Wiener–Khinchin theorem, it provides an accurate discrete analog of the continuous autocovariance Equation (A.7), valid for finite-length, evenly spaced datasets. This function quantifies how the Doppler noise is correlated as a function of time lag and forms the basis for constructing the covariance matrix R used in the whitening procedure described below.

The vector $\bar{R}_{y,1}$ defines the "normalized" autocovariance vector for a specific noise type, depending on its spectral exponent α. Finally, the normalized covariance matrix $\bar{R}$ for each individual noise source is given by a Toeplitz matrix:

$$\bar{R}_{pq} = \bar{R}_{y,1}(\tau(p-q+1), \tau); p, q = 1,\ldots,\frac{N}{2}+1, \quad (31)$$

where each descending diagonal from left to right is constant. This structure reflects the assumption that correlations depend only on the temporal separation between samples, not on their absolute position in time.

In general, to obtain the noise covariance matrix R for a specific noise source, each element of the normalized matrix $\bar{R}$ must be scaled individually:

$$R_{pq} = \sqrt{h_y(t_i)h_y(t_j)}\,\bar{R}_{pq}. \quad (32)$$

For stationary noise (i.e., all other noise sources in the VERITAS case except plasma and troposphere), R is instead obtained by simply scaling the normalized version by h_y:

$$R = h_y\bar{R}. \quad (33)$$

The noise sources are characterized by expected levels of Allan variances, say, $\sigma_y^2(\tau)$. From Equation (A.29), the expected spectral amplitudes h_y are computed by solving, for a given component,

$$\sigma_y^2(\tau) = \frac{2h_y}{N\Delta t(\pi\tau)^2}\sum_{s=2}^{N/2} \nu_s^{\alpha-2}\sin^4\left[\frac{\pi(s-1)\tau}{N\Delta t}\right]. \quad (34)$$

The AVAR of a Doppler noise dataset generated by the TK algorithm with h_y given by Equation (34) corresponds, statistically, to $\sigma_y^2(\tau)$.

In the cases of plasma and the troposphere, Equation (34) must be solved at each epoch as $h_y = h_y(t)$ (Equations (15) and (18), respectively).

In practical applications to real tracking data, the noise model parameters are estimated from the residuals. Specifically, the PSD of the residual Doppler time series is computed, and the spectral slope α and spectral amplitude h_y are derived by a linear least-squares fitting in the log–log domain. Indeed, this can lead to an imperfect retrieval of noise parameters, which may affect the reconstructed noise covariance matrix. When multiple slopes are observed, the PSD can be segmented and separate α fitted accordingly. As discussed in Section 2.3, in this work, rather than applying each α only over the τ interval where it is observed, we assume that each spectral behavior is valid over the entire τ range considered. Consequently, in the pseudocode of Table 3, step 1 must be repeated also for every spectral exponent α (i.e., every color) associated with that noise source.

The full covariance matrix R is then constructed by summing the individual matrices corresponding to each independent noise component. Finally, the Cholesky decomposition is applied to retrieve the whitening matrix V, enabling the transformation required to properly filter correlated

Table 3
Pseudocode for the Computation of Noise Covariance Matrix and Whitening Transformation

Inputs:
- τ: integration time
- N: number of data points, spaced by τ
- σ_y^2: Allan deviation for each noise source
- α: spectral exponent for each noise source

Procedure:
1 For each noise source and each associated spectral exponent α
  1.1 Assume a PSD of the form $S_y(f) = h_y f^{\alpha}$
  1.2 Compute the normalized autocovariance vector $\bar{R}_{y,1}$ using Eq. (30)
  1.3 Construct the normalized covariance matrix $\bar{R}$ as a Toeplitz matrix with Equation (31)
  1.4 Compute the spectral amplitude h_y by solving Equation (34) for the given σ_y^2
  1.5 Scale the normalized covariance matrix according to Equations (32) or (33) for stationary noise
2 Construct the total covariance matrix combining the contributions from all independent noise sources: $R = \sum_k R_k$
3 Whitening transformation
  3.1 Apply the Cholesky decomposition $R = VV^T$
  3.2 Compute the whitened quantities: $\tilde{y} = V^{-1}y$, $\tilde{H} = V^{-1}H$
  3.3 Proceed with the filtering using $\tilde{y}$ and $\tilde{H}$

Output:
- Full covariance matrix R
- Whitening matrix V
- Whitened observation $\tilde{y}$

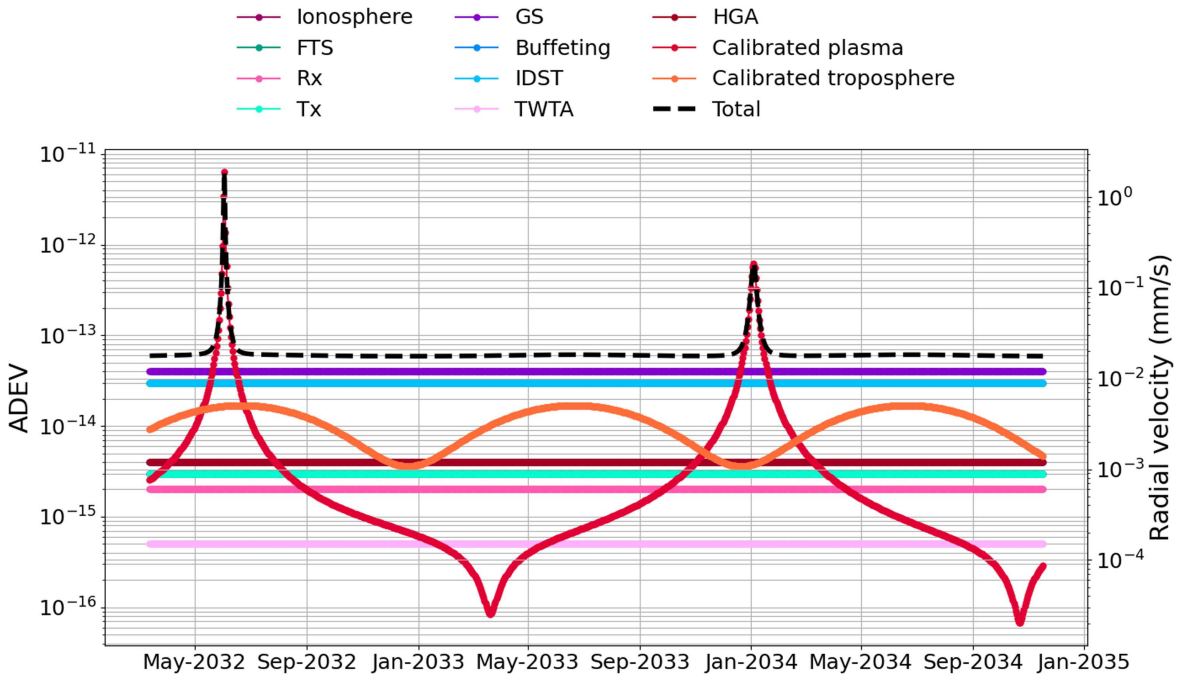


Figure 1. VERITAS Doppler error budget at $\tau = 10$ s integration time, for a trajectory with launch in 2029. The total ADEV is shown along with contributions from individual noise sources. For plasma and troposphere components, only the calibrated curves are reported.

Doppler data (see Section 4). Note that the autocovariance vector contains $N/2 + 1$ elements only (see Appendix A). This means that it can be used to whiten a noise sequence of $N/2 + 1$ samples. Consequently, to whiten a dataset of duration T (e.g., 12 hr), the autocovariance must first be computed over twice that duration (e.g., 24 hr), ensuring that the required half-length vector is available.

5. VERITAS Mission: The Gravity Science Experiment

To address its scientific objectives, VERITAS will carry an X-band interferometric Synthetic Aperture Radar called Venus Interferometric Synthetic Aperture Radar (VISAR; S. Hensley et al. 2020), a near-infrared imaging spectrometer called the Venus Emissivity Mapper (VEM; J. Helbert et al. 2020), and a gravity science experiment. The VERITAS gravity science experiment will be conducted during Science Phase 2 of the mission, which is nominally planned to last four Venusian cycles. During this phase, the spacecraft will operate in a near-polar, near-circular, low-altitude orbit (inclination ~85°, orbit period ~91 minutes, mean orbit altitude ~218 km). A dual-frequency two-way coherent radio link in X and Ka bands will be established from NASA's Deep Space Network antenna to the spacecraft's Integrated Deep Space Transponder. Radio tracking data will consist of both Doppler and range observables, acquired for approximately 8 hr per day, at least 5 days per week (S. Smrekar et al. 2022).

Previous numerical simulations of this experiment, based on the assumption of white noise, predict that VERITAS will achieve a gravity field spatial resolution between 85 and 120 km, with 90% of the planet mapped at a resolution better than 106 km (F. Giuliani et al. 2025).

To evaluate the impact of colored noise on the VERITAS gravity science investigation, specifically on the estimation of Venusian gravity field parameters such as the spherical harmonic coefficients, and to validate the results obtained in F. Giuliani et al. (2025), numerical simulations were conducted using JPL's orbit determination software MONTE (S. Evans et al. 2018). Range data were excluded from these simulations since previous analyses have shown that they contribute minimally to the gravity field recovery.

Table 4
Doppler Noise Sources and Corresponding ADEV Values at $\tau = 10$ s for VERITAS Mission, Assuming a Launch in 2029

Noise Sources	ADEV at $\tau = 10$ s
Plasma	$6.8 \times 10^{-17} - 6.3 \times 10^{-12}$
Troposphere	$3.6 \times 10^{-15} - 1.7 \times 10^{-14}$
Ionosphere	3×10^{-15}
Frequency and timing system (FTS)	3.7×10^{-14}
Receiver chain (ground, Rx)	2.1×10^{-15}
Transmitter chain (ground, Tx)	3×10^{-15}
Ground station antenna (GS)	4×10^{-14}
Spacecraft buffeting	4×10^{-14}
Integrated deep space transponder (IDST)	3×10^{-14}
Traveling wave tube amplifier (TWTA)	5×10^{-16}
Spacecraft high-gain antenna (HGA)	4×10^{-15}

Note. The Doppler error budget follows the model described in Section 2 (adapted from S. W. Asmar et al. 2005; L. Iess et al. 1983, 2014; F. Giuliani et al. 2025).

5.1. Doppler Noise Budget

To model the VERITAS Doppler noise budget, we considered all relevant error sources described in Section 2, including propagation media and both onboard and ground instrumentation. Figure 1 illustrates the total Doppler ADEV, along with the contributions from individual noise sources, for Science Phase 2 of the VERITAS mission, assuming a launch in 2029. Table 4 summarizes the modeled ADEV at $\tau = 10$ s for each noise source.

The Doppler noise floor for VERITAS is approximately 18 μm s^{-1} at 10 s. However, the total noise is time variable

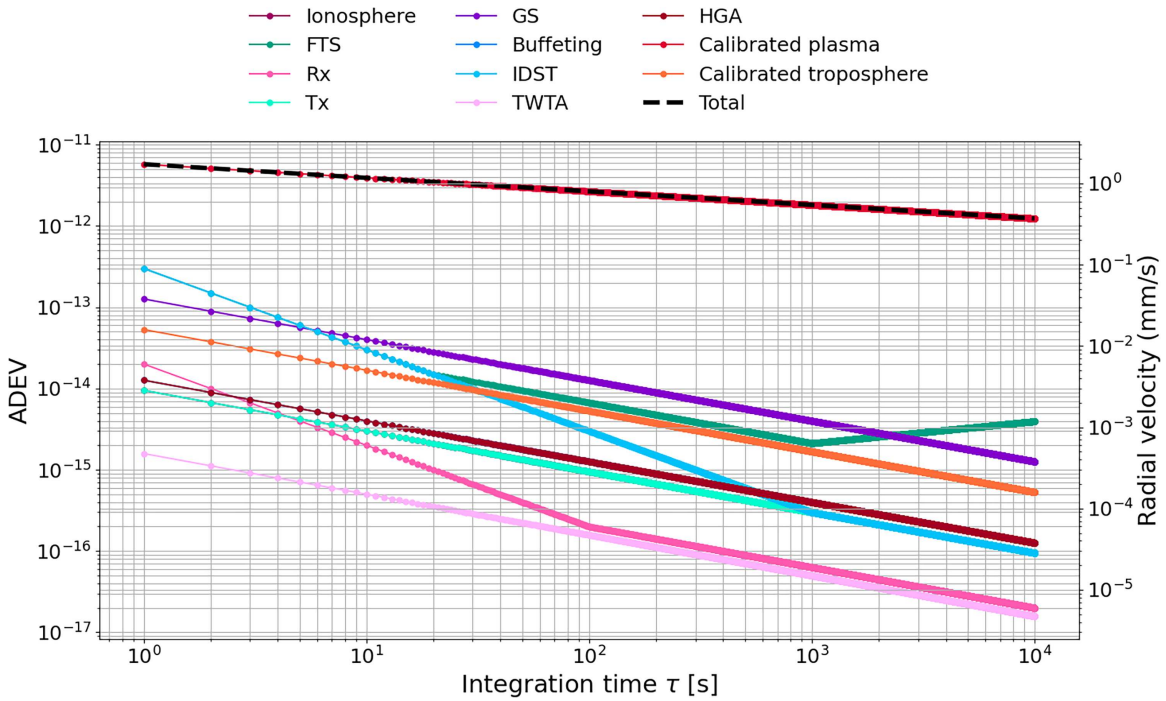


Figure 2. ADEV vs. integration time τ for an epoch near a superior solar conjunction. The dominant noise is the plasma, and the total Doppler noise is colored.

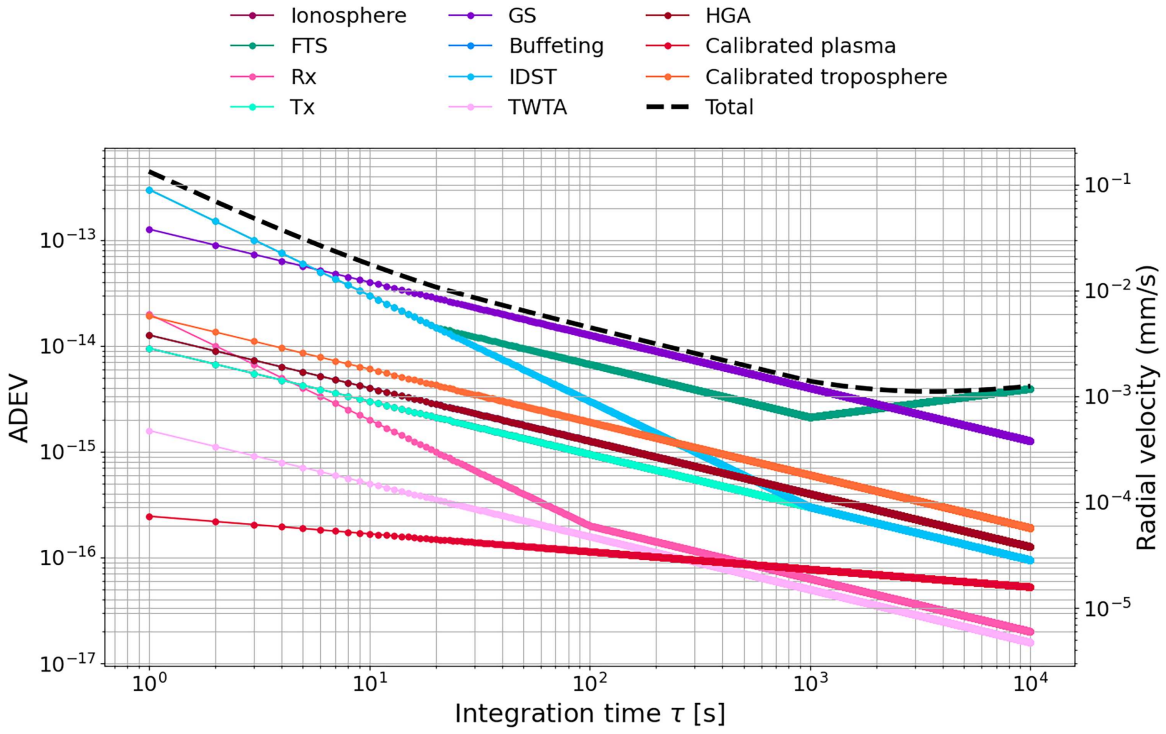


Figure 3. ADEV vs. integration time τ for an epoch far from any superior solar conjunction. In this condition the total Doppler noise is almost white.

owing to the dependence of plasma noise on SPE angle and the seasonal variations in tropospheric noise. Plasma noise (see Section 2.1), in particular, exhibits two distinct peaks corresponding to superior solar conjunctions, when the SPE angle is small. Nevertheless, the dual-frequency link architecture (X and Ka bands on both uplink and downlink) allows for partial calibration of the plasma, reducing its contribution by approximately 75% (G. Mariotti & P. Tortora 2013). In addition, the use of water vapor radiometers can provide significant reduction (∼95%; D. R. Buccino et al. 2021) of the tropospheric noise. Contributions from the Venus ionosphere and atmosphere are not included in the modeling, as their impact will be mostly limited to the time near ingress and egress from occultations, affecting only a limited number of data points (∼7%).

Figures 2 and 3 show the ADEV as a function of the integration time τ for each individual noise source. Figure 2 corresponds to an epoch near a solar superior conjunction,

where plasma noise remains the dominant contributor despite partial calibration. Figure 3 refers to a more favorable geometry, where the solar contribution is reduced; in this condition the total Doppler noise has a nearly white spectrum. From Figure 1 it can be observed that the ADEV exceeds the nominal noise floor ($18\,\mu m\,s^{-1}$) by more than a factor of two during only approximately 5% of the science phase. Therefore, for the VERITAS case, the presence of colored noise is not expected to significantly affect the results since the dominating noise sources are expected to be white for most of the time.

5.2. Dynamical Model

The dynamical modeling adopted for the VERITAS orbit determination is designed to account for all relevant gravitational and nongravitational forces affecting the radio link at or near the level of the measurement noise. The gravitational attractions of the major solar system bodies are included considering only their monopole term (point mass). Venus's gravity field, however, is modeled with a spherical harmonic expansion up to degree and order 220. The gravitational potential at a point outside Venus's reference radius R, expressed in spherical coordinates (r, θ, φ), is given by (W. M. Kaula (1966)

$$U(r,\theta,\varphi)=\frac{GM}{r}\left[1+\sum_{l\geqslant 2}\left(\frac{R}{r}\right)^{l}\sum_{m=0}^{l}\bar{P}_{lm}(\cos\theta)\left(\bar{C}_{lm}\cos m\varphi+\bar{S}_{lm}\sin m\varphi\right)\right]. \quad (35)$$

In this expression, GM is Venus's gravitational parameter, r is the radial distance from the planet's center, θ is the colatitude, and φ is the longitude. The terms $\bar{C}_{lm}$ and $\bar{S}_{lm}$ are the fully normalized spherical harmonic coefficient of degree l and order m, while the functions $\bar{P}_{lm}$ are the fully normalized associated Legendre polynomials. In addition to the static gravity field, the model also includes perturbations due to Venus's solid-body tides, parameterized by the tidal Love number k_2, as well as atmospheric tides, which are modeled introducing periodic corrections to the gravity field coefficients (G. Cascioli et al. 2021, 2023). The nominal gravity field adopted in this study was constructed by blending two complementary datasets. As discussed in F. Giuliani et al. (2025), at low degrees, we use the MGNP180U gravity field model (A. S. Konopliv et al. 1999), which incorporates the best available information from Magellan tracking data. However, its resolution is limited by data coverage and the regularization techniques applied during inversion, and it is only defined up to degree and order 180. For these reasons, we complement MGNP180U with gravity coefficients inferred from topography, computed using the analytical formulation and the spherical harmonic expansion of Venus's topography provided by M. A. Wieczorek (2015) for degrees above $l_0 = 80$. A smooth transition was applied between the two datasets to ensure continuity, implemented by blending the MGNP180U and topography-derived coefficients with a weighting function. Specifically the coefficients were constructed as $C_{lm} = \sqrt{\alpha}\,C_{lm}^{\text{topography}} + \sqrt{1-\alpha}\,C_{lm}^{\text{gravity}}$, where $C_{lm}^{\text{topography}}$ are the coefficients from topography, C_{lm}^{gravity} are the MGNP180U gravity coefficients, and $\alpha = \frac{l-l_0}{l_{\max}-l_0}$. A different approach may be used, which, however, will not impact the whitening procedure we are presenting.

Nongravitational forces are also included in the force model: solar radiation pressure and atmospheric drag, modeled using an exponential density profile compatible with the Venus Global Reference Atmospheric Model (Venus-GRAM; H. Justh et al. 2006). Drag acceleration and solar radiation pressure both depend on the spacecraft shape, which we modeled as a central cylindrical bus with a parabolic dish to represent the high-gain antenna, along with a plate for the VISAR antenna and two plates for the solar panels. We also account for wheel desaturation maneuvers, while our model neglects Venus albedo and infrared emission. A more detailed description of the dynamical model is provided in F. Giuliani et al. (2025).

5.3. Estimation Filter Setup

To estimate the parameters of interest and assess their uncertainties, we used ORACLE, a weighted least-squares proprietary filter with a priori information, external to MONTE. This filter has already been successfully employed in the orbit determination of past interplanetary missions such as Cassini and Juno (L. Iess et al. 2018, D. Durante et al. 2019, D. Durante et al. 2020).

Our simulations adopt a multiarc approach, well suited for long-duration missions. The total time span of tracking data is divided into 279 shorter and nonoverlapping intervals called arcs, with each arc spanning 2 or 3 days in our case. In a multiarc approach, the estimated parameters are grouped into two categories: local parameters, which are specific to each arc, and global parameters, which are common to all arcs (A. Milani & G. Gronchi 2009).

The local parameters include, besides the spacecraft's position and velocity at the beginning of the arc, the velocity change associated with wheel off-loading maneuvers (M. S. Wallace et al. 2019), a scale factor for the solar radiation pressure, and one empirical along-track acceleration per orbit to compensate for mismodeled nongravitational forces, mainly due to uncertainties in Venus's atmospheric density over the orbit period (A. M. Gargiulo et al. 2024). Moreover, to account for possible short-term variations in Venus's spin rate observed by J. L. Margot et al. (2021), we also estimate arc-specific values for the prime meridian angle at a reference epoch and the sidereal angular rotation rate (G. Cascioli et al. 2021; F. Giuliani et al. 2025).

The list of global parameters includes Venus's gravitational parameter, the coefficients of the spherical harmonic expansion of its gravity field up to degree and order 180, and

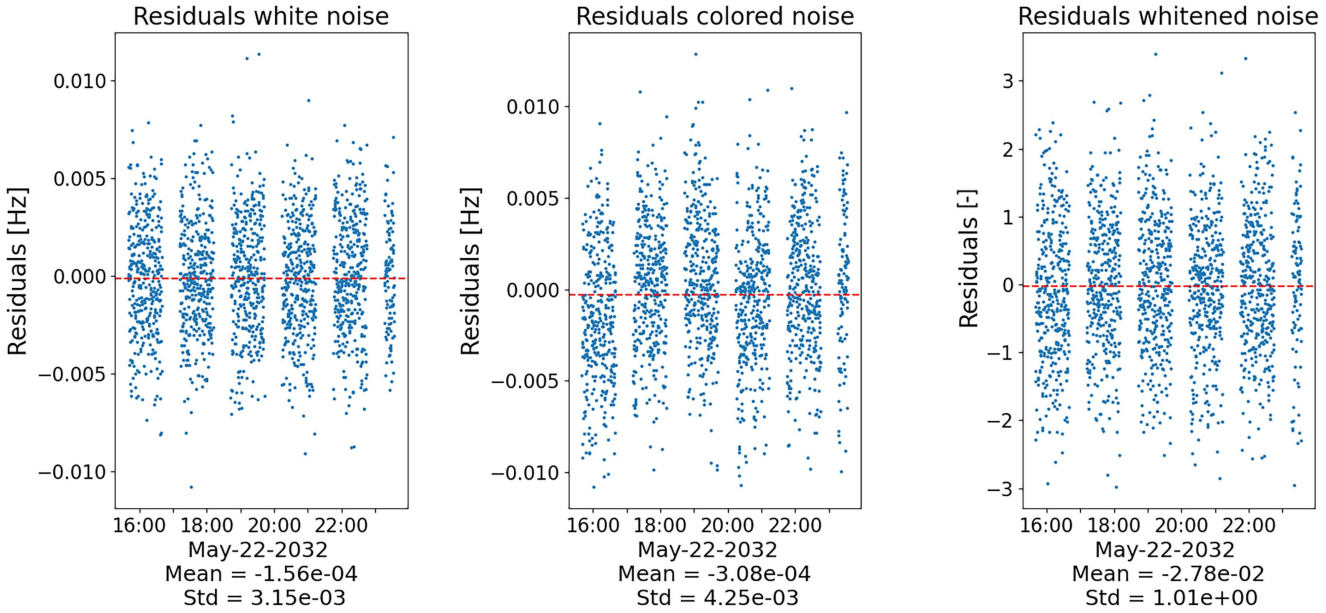


Figure 4. Doppler residuals for the first tracking pass of arc 22 in the three simulated cases: white noise (left), colored noise without whitening (middle), and colored noise with whitening applied (right). The red line indicates the mean value.

Table 5
VERITAS Gravity Science Experiment Estimation Filter Setup

Parameter	A Priori Value	A Priori Uncertainty
Local Parameters		
Spacecraft initial position	From trajectory kernel	0.1 km
Spacecraft initial velocity	From trajectory kernel	1 cm s^{-1}
Solar radiation pressure scale factor	1	0.25
Δv WoL	0	0.5 mm s^{-1}
Along-track acceleration (1 per orbit)	0	9×10^{-4} mm s^{-2}
Sidereal period	From IAU (B. A. Archinal et al. 2018)	61 ppm (J. L. Margot et al. 2021)
Global Parameters		
Gravity field coefficients	See section 6.2	Kaula's rule
Pole R.A. and decl.	From IAU (B. A. Archinal et al. 2018)	1°
Pole R.A. and decl. rate	G. Cascioli et al. 2021	1°
Venus's gravitational parameter	324, 858.592 km^3 s^{-2} (A. S. Konopliv et al. 1999)	6×10^{-3} km$^3 s^{-2}$ (A. S. Konopliv et al. 1999)
Love number k_2 (real)	0.295 (A. S. Konopliv & C. F. Yoder 1996)	0.066 (A. S. Konopliv & C. F. Yoder 1996)
Love number k_2 (imaginary)	0	0.1

Note. The table lists all estimated parameters along with their a priori values and uncertainties.

Venus's pole orientation, estimating the R.A. and decl. at a reference epoch. Although the gravity field is modeled up to degree and order 220, the estimation is limited to degree and order 180 to reduce computational cost. Additionally, the real and imaginary parts of the tidal Love number k_2 are included among the estimated parameters.

A priori values and associated uncertainties for both local and global parameters are summarized in Table 5. For the gravity field coefficients, the a priori uncertainties follow Kaula's empirical rule (W. M. Kaula 1966), which models the power-law decays of gravity field amplitudes for solid planetary bodies. According to this rule, the amplitude spectrum of the gravity field, defined as

$$C_l = \sqrt{\frac{\sum m \quad \left(C_{lm}^2 + S_{lm}^2\right)}{2l+1}}, \tag{36}$$

is assumed to decay as

$$C_l = \frac{K}{l^2}. \tag{37}$$

The proportionality constant K, which varies depending on the body, is set to 2×10^{-5} in this work.

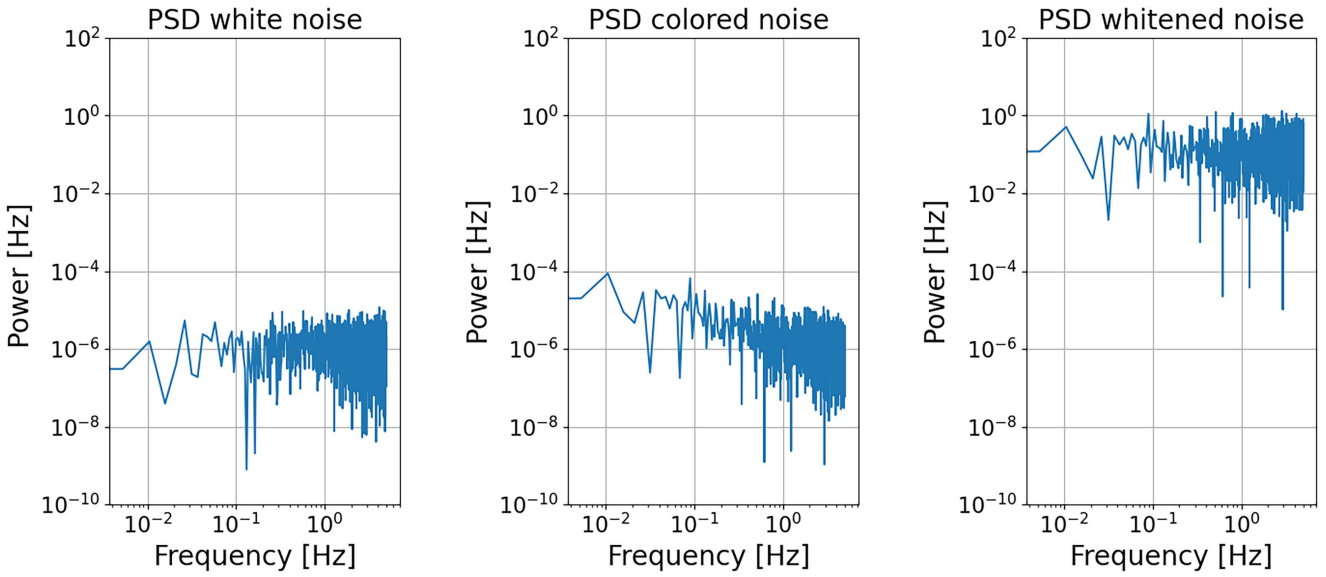


Figure 5. PSD of the residuals for the first pass of Arc 22 for the three noise scenarios: white noise (left), colored noise without whitening (middle), and colored noise with whitening applied (right). For the white noise and whitened colored noise cases, the flat spectra indicate white-noise behavior. Moreover, we verified that the standard deviation of the PSD matches its mean, consistent with Equation (13) of J. Timmer & M. Konig 1995). In contrast, the nonwhitened colored noise exhibits a decaying trend typical of red noise.

6. Results and Discussion

To evaluate the impact of colored noise on parameter estimation and to quantify the potential biases introduced when such noise is not properly whitened before filtering, three simulation scenarios were considered: (1) White noise was added to the observables, and data were processed in the filter. (2) Colored noise was added to the observables, but no whitening was applied before filtering; in this case, the observation uncertainties were set equal to the standard deviation of the residuals (i.e., the normal Doppler processing, where noise is assumed to be white). (3) Colored noise was added to the observables, corrected with the whitening procedure, and the data were then processed through the filter.

We will first present the results for the application of these steps to a pass of a specific arc (Section 6.1) and then discuss the outcomes for the gravity field estimation (Section 6.2). Additionally, Section 6.3 presents the same results using a Doppler error budget in which the contribution of the Ka band to plasma noise is not considered.

6.1. Whitening Procedure for a Test Pass

To illustrate the effects of applying the whitening procedure on the residuals, ACF, and PSD, we present the results for the first tracking pass of arc 22. This arc was selected because, being close to a superior solar conjunction, the "red" plasma noise dominates the error budget, making it particularly suitable for highlighting the influence of colored noise.

Figure 4 shows the residuals obtained for this pass across the three scenarios. When colored noise is introduced without whitening, the residuals display a characteristic signature of red noise (see PSD and ACF in Figures 5 and 6, respectively). In contrast, after applying the whitening procedure, the residuals exhibit the expected features of whitened data: zero mean, unit variance, and no signature, as described in Section 4.

Figure 5 presents the corresponding PSDs. For the white noise and whitened colored noise cases, the flat spectra indicate white noise behavior, with no frequency-dependent structure. However, in the case where colored noise is not whitened, the PSD follows a decaying trend typical of red noise, as expected given the dominant plasma contribution.

Finally, Figure 6 shows the ACFs of the residuals. In the unwhitened colored noise case, significant correlations persist over long lags, while they are essentially absent in the white noise and whitened colored noise cases, as expected.

These results confirm that the whitening procedure successfully normalizes the residuals, flattens the PSD, and removes correlations in the data, as anticipated. Consequently, after this step, observation can be processed through the usual orbit determination estimation filter.

6.2. Gravity Field Recovery

Figure 7 shows the uncertainty and error of the gravity field spectra for the three scenarios previously defined (white noise, colored noise, and colored noise with whitening applied). Both the estimated errors and formal uncertainties are plotted as a function of spherical harmonic degree. The formal uncertainty of the amplitude spectra C_l at each degree is computed through the linear propagation method (G. Cascioli et al. 2024):

$$\sigma_{C_l}^2 = \frac{\partial C_l}{\partial x} P \frac{\partial C_l}{\partial x}^T, \tag{38}$$

where x is the vector that contains the spherical harmonic coefficients from degree 2 to degree l. The error spectrum is instead computed as the difference between the estimated C_l and the one computed from our reference gravity model.

In each noise scenario, the estimated error and the formal uncertainty curves are consistent. This is further confirmed in Figure 8, where the histograms of the ratio between estimated errors and formal uncertainties are well represented by a Gaussian distribution with zero mean and unit standard

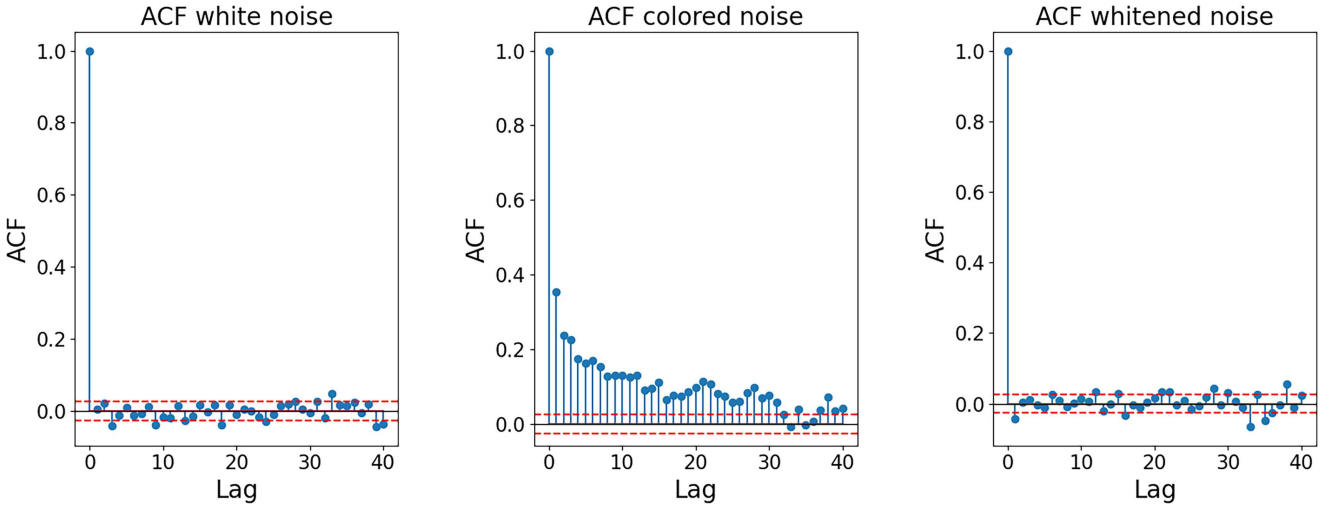


Figure 6. ACFs of the residuals for the first pass of arc 22 for the three simulated cases: white noise (left), colored noise without whitening (middle), and colored noise with whitening applied (right). The lag axis is truncated at 40. Lag is expressed in number of samples.

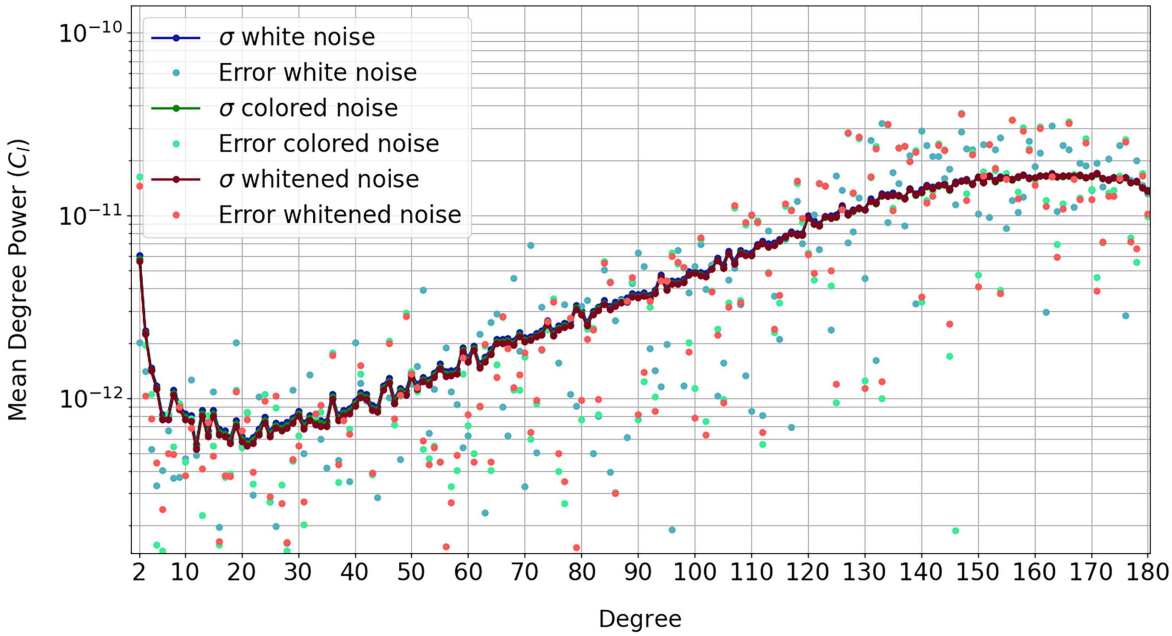


Figure 7. Spectrum of gravity field uncertainty and error for the white noise, colored noise, and prewhitened noise case. Both formal uncertainties and estimated errors are plotted.

deviation. Moreover, the comparison across the three cases shows no significant differences in either errors or uncertainties.

Complementing this result, Figure 9 shows the gravity anomaly uncertainty at degree 180, which reflects how gravity will be mapped across the planet. The three maps exhibit no significant differences, as also illustrated by the difference maps comparing the colored noise and whitened noise scenarios to the white noise case. This is further confirmed by the reported rms, mean, and maximum uncertainties computed over 90% of Venus's surface, supporting the conclusion that the mapping capability remains unaffected by colored noise for VERITAS.

In addition to the gravity field, we also examined parameters related to Venus's rotational state and tidal response. The uncertainties in these parameters show no meaningful variation across the three scenarios. Table 6 presents a comparison of the estimated uncertainties—including the R.A. (α) and decl. (δ) of Venus's pole, the moment of inertia factor (MOIF), the obliquity (ϵ), the precession rate (Ω), the tidal Love number (k_2), and the tidal phase lag (δk_2)—alongside current best estimates and VERITAS mission requirements.

These results confirm that the assumption of white noise in the context of the VERITAS mission is acceptable, as expected given that the overall Doppler noise is close to white for almost 95% of the time.

6.3. Results for a Doppler Error Budget Considering Only X Band for Plasma Noise

To assess how the parameter estimation is affected when colored noise dominates the Doppler noise budget for a significant portion of the mission, we repeated the analysis for

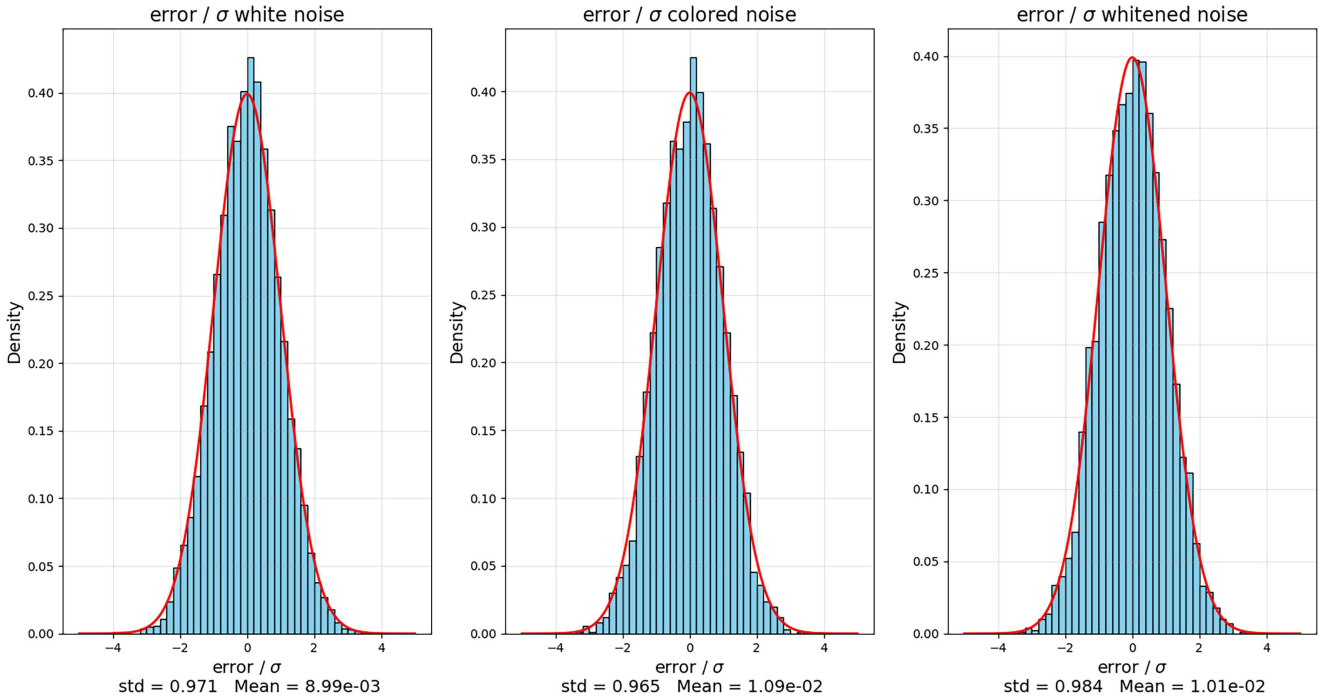


Figure 8. Histogram of the ratio between estimated errors and formal uncertainties for the white noise, colored noise, and whitened noise cases. For reference, a red curve shows the standard Gaussian distribution. The mean and standard deviation of each case are also reported. Only coefficients up to degree 70 are included, since the lower degrees are the most affected by noise, while at higher degrees the solution is dominated by the Kaula constraint.

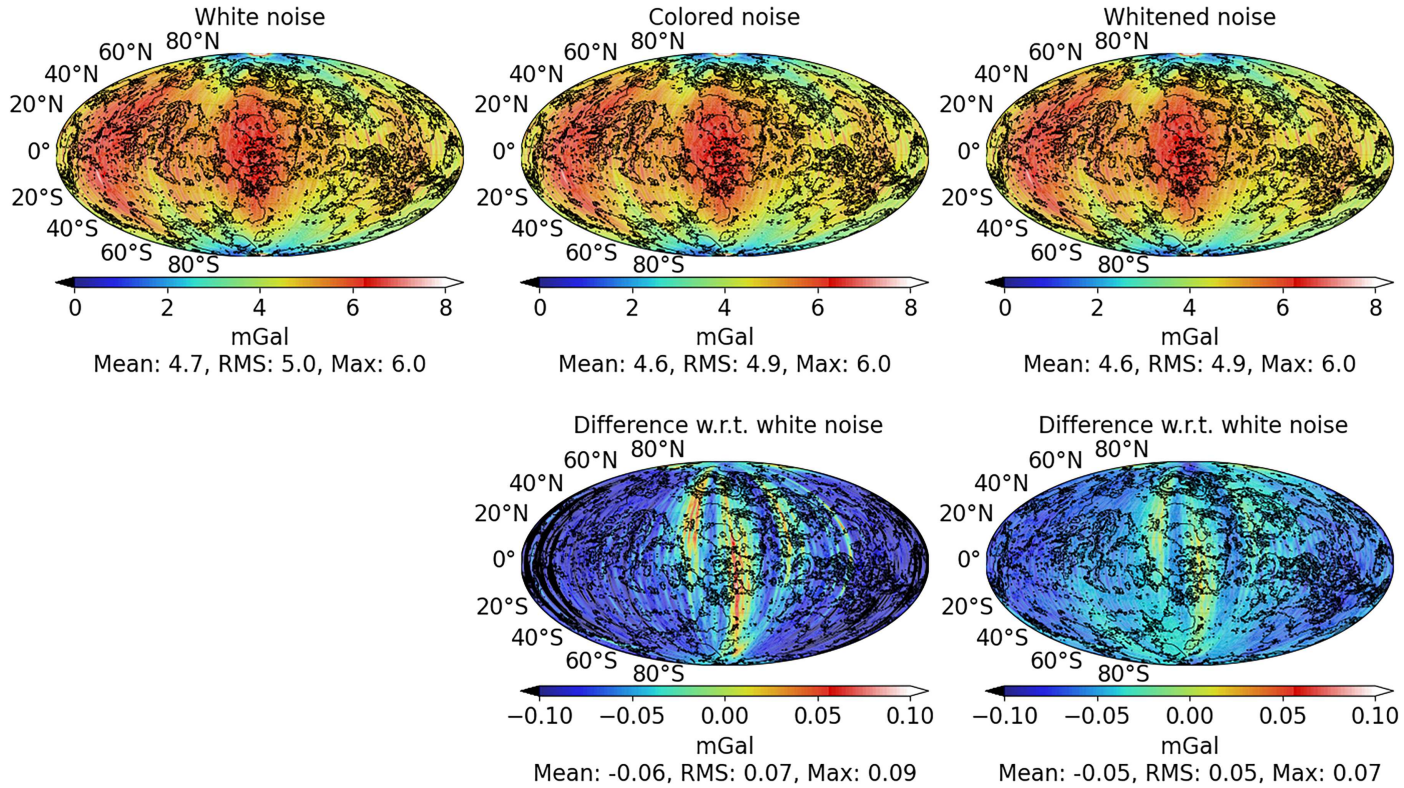


Figure 9. Gravity anomaly uncertainty at degree 180 for the three noise scenarios (top row) and differences with respect to the white noise scenario (bottom row). The rms, mean, and maximum computed over 90% of Venus's surface are also reported.

an X-band radio link (7.2 GHz uplink, 8.4 GHz downlink). In this scenario, plasma noise is treated as uncalibrated (i.e., $P_{\text{calib}} = 0$ in Equation (15)). As a result, the plasma noise ranges in this case from 5.3×10^{-15} to 4.9×10^{-10} depending on the SPE angle. All other noise sources are assumed unchanged.

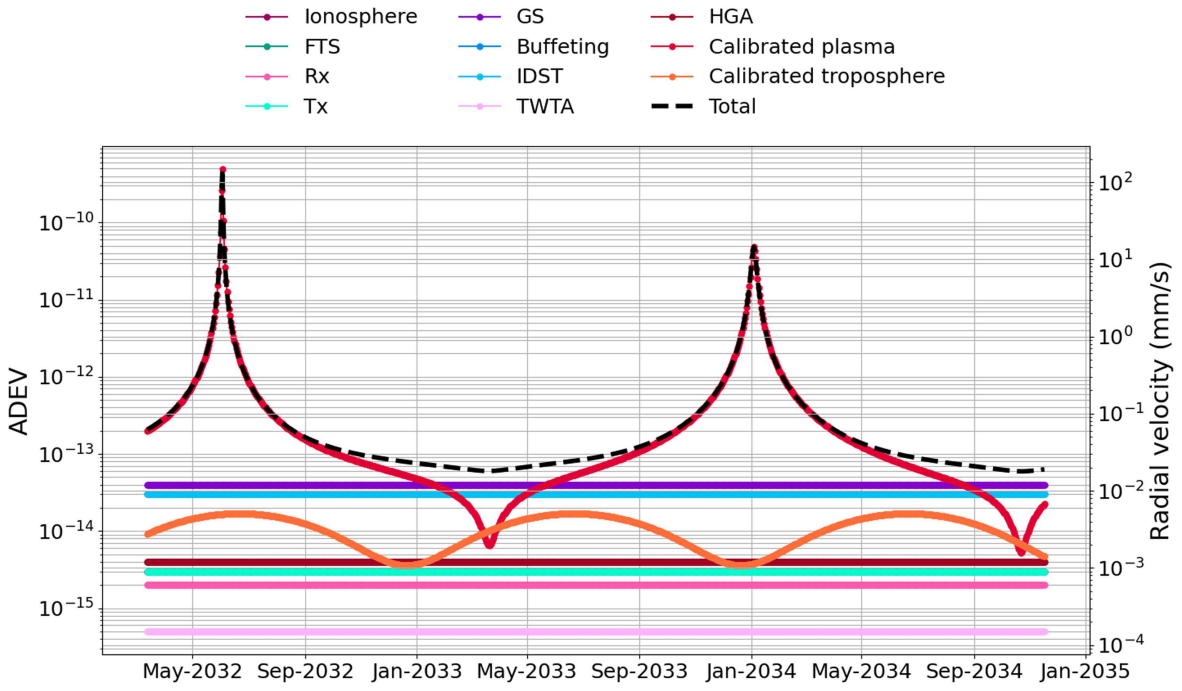


Figure 10. VERITAS Doppler error budget at $\tau = 10$ s integration time assuming only X-band tracking for plasma (i.e.,$P_{\rm calib} = 0,\ \nu_0 = 7.8$ GHz in Equation (15)).

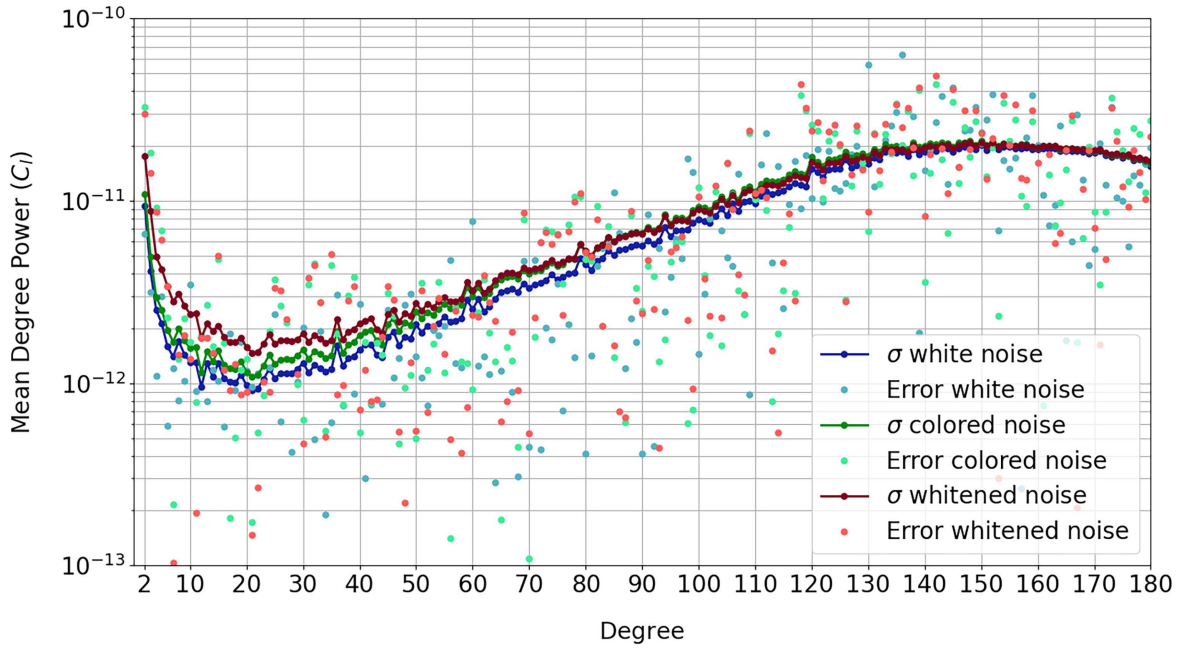


Figure 11. Gravity field amplitude spectrum assuming only X-band tracking for the plasma noise (i.e., $P_{\rm calib} = 0,\ \nu_0 = 7.8$ GHz in Equation (15)).

Table 6
Comparison of Uncertainties in Venus's Tidal and Rotational Parameters Obtained from the Three Noise Scenarios, Alongside Current Best Estimates and Mission Requirements

	Current Uncertainty	Requirement	White Noise	Colored Noise	Whitened Noise
α_0 (arcsec)	3 (J. L. Margot et al. 2021)	…	0.44	0.43	0.44
δ_0 (arcsec)	2.5 (J. L. Margot et al. 2021)	…	0.25	0.24	0.25
ϵ (arcsec)	3 (J. L. Margot et al. 2021)	…	0.20	0.19	0.20
Ω (deg/century)	9.2×10^{-2} (J. L. Margot et al. 2021)	2.1	5.4×10^{-3}	5.2×10^{-3}	5.4×10^{-3}
MOIF	2.4×10^{-2} (J. L. Margot et al. 2021)	5×10^{-3}	1.5×10^{-3}	1.4×10^{-3}	1.5×10^{-3}
k_2	6.6×10^{-2} $(2-\sigma)$ (A. S. Konopliv & C. F. Yoder 1996))	0.01	2.4×10^{-4}	2.4×10^{-4}	2.4×10^{-4}
δk_2 (deg)	…	0.25	2.9×10^{-2}	2.9×10^{-2}	3.0×10^{-2}

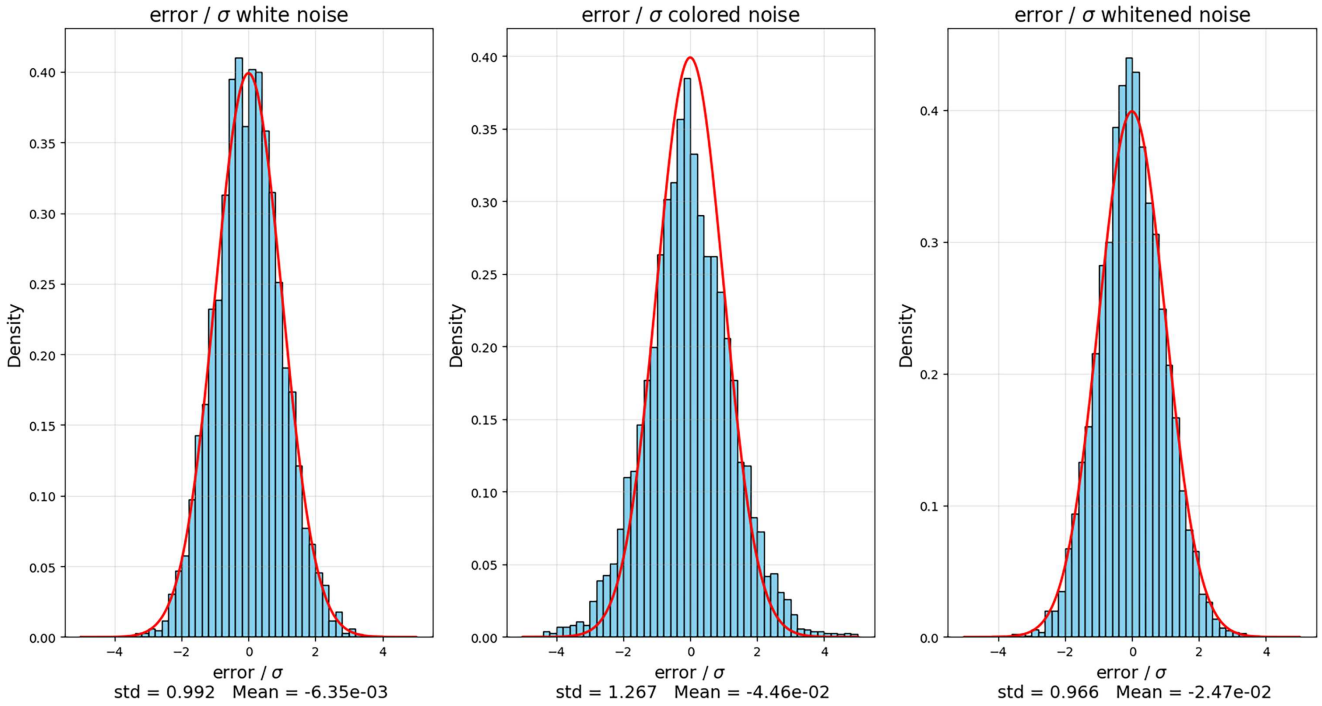


Figure 12. Histogram of the ratio between estimated errors and formal uncertainties for the white noise, colored noise, and whitened noise cases, assuming only X-band tracking for the plasma noise. For reference, a red curve shows the standard Gaussian distribution. The mean and standard deviation of each case are also reported. Only coefficients up to degree 70 are included, since the lower degrees are the most affected by noise, while at higher degrees the solution is dominated by the Kaula constraint.

Table 7
Comparison of Uncertainties in Venus's Tidal and Rotational Parameters Assuming Only X-band Tracking for the Plasma Noise (i.e., $P_{\rm calib} = 0$, $\nu_0 = 7.8$ GHz in Equation (15))

	Current Uncertainty	Requirement	White Noise	Colored Noise	Whitened Noise
α_0 (arcsec)	3 (J. L. Margot et al. 2021)	…	0.94	1.2	2.2
δ_0 (arcsec)	2.5 (J. L. Margot et al. 2021)	…	0.52	0.64	1.2
ϵ (arcsec)	3 (J. L. Margot et al. 2021)	…	0.42	0.51	0.96
Ω (deg/century)	9.2×10^{-2} (J. L. Margot et al. 2021)	2.1	1.1×10^{-2}	1.4×10^{-2}	2.6×10^{-2}
MOIF	2.4×10^{-2} (J. L. Margot et al. 2021)	5×10^{-3}	3.1×10^{-3}	3.8×10^{-3}	7.1×10^{-3}
k_2	6.6×10^{-2} (2σ) (A. S. Konopliv & C. F. Yoder 1996)	0.01	3.9×10^{-4}	4.3×10^{-4}	6.5×10^{-4}
δk_2 (deg)	…	0.25	4.6×10^{-2}	5.1×10^{-2}	7.1×10^{-2}

Figure 10 presents the resulting Doppler error budget. As expected, plasma noise becomes the primary contributor to the total error over large portions of the mission duration.

Figure 11 shows that, under these conditions, both the formal uncertainties and the estimation errors increase in the colored noise case compared to the white noise case, and even more so in the whitened case. This effect is particularly relevant for the low-degree coefficients and for the tidal and rotational parameters, as reported in Table 7. Moreover, Figure 12 indicates that, for the colored noise case, the histogram of error-to-uncertainty ratios deviates slightly from a standard Gaussian distribution, whereas in the other two cases it remains consistent with it.

These results confirm the importance of applying the whitening procedure in the presence of colored noise. Without whitening, the filter underestimates uncertainties and biases the estimation by up to a factor of $\sim$2. Consequently, in the whitened colored noise case, the requirement on the MOIF uncertainty is no longer met. Furthermore, this analysis highlights the importance of Ka-band tracking in reducing plasma noise and ensuring the accurate recovery of Venus's gravity and rotational state.

7. Conclusions

In this work, a practical method has been developed to process correlated Doppler measurement, characterized by frequency-dependent behavior and a full noise covariance matrix, within commonly used orbit determination filters, which typically assume uncorrelated (white) noise and accept only diagonal covariance matrices. The approach is based on the construction of an appropriate noise covariance matrix, starting from the autocovariance function and the PSD associated with each noise source. Through this transformation, the PSD of the measurement noise becomes white, measurements are decorrelated, and residuals are normalized. This ensures the proper estimation of parameters and their associated uncertainties, provided that dynamical and noise models are accurate, an outcome that cannot be guaranteed when colored noise is neglected or improperly treated as white.

The proposed procedure was applied to a realistic case study: the gravity science experiment of the upcoming NASA's VERITAS mission to Venus. Previous simulations had assumed white noise in the evaluation of gravity field recovery and the estimation of tidal and rotational parameters. Here, using comparable dynamical and noise models, three different scenarios were analyzed: Doppler data with white noise, Doppler data with colored noise, and Doppler data with colored noise processed through the prewhitening procedure. The resulting gravity field spectra demonstrate that both the formal uncertainties and estimation errors are comparable in the three cases and consistent across the three cases. Likewise, the uncertainties in the tidal and rotational parameters, as well as gravity anomaly uncertainty maps, exhibit negligible differences. These results confirm that the white noise assumption is adequate for VERITAS, given that the Doppler noise is nearly white for most of the mission. Although the simulations presented here are based on a 2029 launch timeline, no significant impact on the results is expected if the launch date shifts, since the influence of colored noise has been shown to be negligible in this context. VERITAS is currently expected to launch in 2031 or 2032.

The methodology introduced here for treating colored noise is general, and it can be applied to other gravity science experiments. An additional scenario was also analyzed in which Ka-band tracking was unavailable for plasma noise calibration, resulting in significantly increased noise level. This case highlighted that the whitening procedure becomes particularly useful when colored noise sources, such as plasma noise, dominate over extended mission phases. In such contexts, whitening is important to prevent colored noise from leading to biased parameter estimation and incorrect uncertainty assessment, thereby enabling accurate orbit determination. Other sources of error orbit determination (e.g., dynamical model inaccuracies) may still be present, but whitening ensures that noise correlations are not a contributing factor.

Acknowledgments

This is VERITAS contribution No. 9. This work was supported in part by the Italian Space Agency under grant No. 2022–15-HH.1-2024. This research was partially conducted at the Jet Propulsion Laboratory, California Institute of Technology, under contract (VERITAS, 80NM0020F0035) with the National Aeronautics and Space Administration. Work by G. C. was supported by NASA under award No. 80GSFC 24M0006 via the VERITAS project.

Appendix A

In this appendix we describe our method to obtain the covariance matrix for a noise dataset characterized by an arbitrary PSD profile. Our final expression has the benefit of not containing integrals, and it is not constrained by the choice of cutoffs in the limits of integrations.

We briefly resume the usual approach. We start from the (power) autocovariance $R_\epsilon(t)$ of a given continuous function $\epsilon(t)$ defined as

$$R_\epsilon(t) = \lim_{T\to+\infty} \frac{1}{2T}\int_{-T}^{T} \epsilon^*(t')\,\epsilon(t'+t)\quad dt', \tag{A.1}$$

where "$\star$" indicates complex conjugation.

For the Wiener–Khinchin theorem, $R_\epsilon(t)$ and the PSD of $\epsilon(t)$, say, $S_\epsilon(f)$, are a Fourier transform (FT)/inverse FT couple.

In particular, if $\epsilon(t)$ is real and $S_\epsilon(f)$ is a single-sided spectrum, we have

$$\begin{aligned} R_\epsilon(t) &= \int_0^{+\infty} S_\epsilon(f)\cos(2\pi tf)\,df; \\ S_\epsilon(f) &= \int_0^{+\infty} R_\epsilon(t)\cos(2\pi tf)\,dt. \end{aligned} \tag{A.2}$$

Using the translation property of the Fourier analysis and Equation (A.2), one finds the following expression for the autocovariance of $y_1(t)$:

$$R_{y,1}(t,\,\tau) = \int_0^{+\infty} S_y(f)\frac{\sin^2(\pi\tau f)}{(\pi\tau f)^2}\cos(2\pi tf)\,df, \tag{A.3}$$

where $R_{y,1}(t=0,\,\tau)$ is the variance of $y_1(t)$.

Suppose that the same physical process is at the origin of each generation of the noise function $x(t)$ and that the mathematical expression of the PSD of $x(t)$, say, $\bar{S}_x(f)$, is known. By introducing it into Equation (A.2), one obtains the expected autocovariance function

$$\langle R_x(t)\rangle = \int_{+\infty}^{0} \bar{S}_x(f)\cos(2\pi tf)\,df; \tag{A.4}$$

if the noise is sampled with time spacing Δt, the corresponding expected covariance matrix is

$$R_{ij} = <R_\epsilon[\Delta t(i-j)] > i,\, j = 1,\ldots, \tag{A.5}$$

and, in principle, it can be used as a whitening filter for all noise datasets $x(t = i\Delta t)$ (R. Mackenzie & W. M. Folkner 2006).

As anticipated in Section 2, we will assume that the expected PSD of $y(t)$ can be modeled by a power law

$$\bar{S}_y(f) = h_y f^\alpha. \tag{A.6}$$

Inserting Equation (A.6) into Equation (A.3), and after substituting $z = \pi f\tau$, we find (for simplicity we omit the angle brackets)

$$R_{y,1}(j\tau,\,\tau,\,\alpha) = \frac{h_y}{\pi^{\alpha+1}}\tau^{-\alpha-1}\int_{\pi\tau f_{\rm inf}}^{\pi\tau f_{\rm sup}} \cos(2jz)\frac{\sin^2 z}{z^{2-\alpha}}dz, \tag{A.7}$$

where $j = t/\tau > 0$. We inserted upper and lower limits of integrations, in principle different from 0 and $+\infty$ (see below). On the contrary, in the domain $z \in [0,\,+\infty]$, the integral into Equation (A.7) is convergent on a very restricted interval corresponding to $-1 < \alpha < +1$ ($\forall\ j \geqslant 0$).

For the expected AVAR (Equation (5)) we find

$$\sigma_y^2(\tau) = \tau^{-\alpha-1}\frac{2h_y}{\pi^{\alpha+1}}\int_{\pi\tau f_{\rm inf}}^{\pi\tau f_{\rm sup}} \frac{\sin^4 z}{z^{2-\alpha}}dz, \tag{A.8}$$

which is convergent, in the domain $z \in [0,\,+\infty]$, for $-3 < \alpha < +1$ (for more details see De Marchi et al. 2024).

Expected variance (Equation (A.7, with $j = 0$) and AVAR (Equation (A.8)) are proportional to $\tau^{-\alpha-1}$. This is true only if integrals converge in the domain $z \in [0,\,+\infty]$; otherwise, the dependence on τ is also present into the integral.

Finally, in the domain $z \in [0,\,+\infty]$ and for $-1 < \alpha < +1$, from Equation (A.7) the expected ACF is given by a simple

formula,

$$U_{y,1}(j) = \frac{R_{y,1}(j\tau,\,\tau,\,\alpha)}{R_{j,1}(0,\,\tau,\,\alpha)} = \frac{1}{2}\,|j-1|^{1-\alpha} - j^{1-\alpha} + \frac{1}{2}(j+1)^{1-\alpha} \tag{A.9}$$

(R. Mackenzie & W. M. Folkner 2006, P. Kuchynka et al. 2014).

A real signal has a finite duration T and is not continuous, but it is composed by a set of data points spaced by Δt. This means that the information about the spectral content for frequencies below $1/T$ and above the Nyquist frequency $1/(2\Delta t)$ is lost or assumed to be negligible. Therefore, one can impose as lower and upper limits to the integrals into Equations (A.7) and (A.8) $z_{\rm inf} = \pi\tau/T$ and $z_{\rm sup} = \pi\tau/(2\Delta t)$. However, these values are just indicative, as they are related to a rough discretization of the continuous function $y_1(t)$.

To bypass this problem, we calculate the expected autocovariance directly in the discrete domain.

A.1. Generalized TK Algorithm

Here we briefly describe the TK algorithm, generalized to an arbitrary PSD profile and not only to power laws. As a first step, we will generate a set of N (even) phase measurements x_r, spaced by an interval of time Δt, by starting from a discrete FT (DFT) vector X_s whose square modulus with appropriate rescaling (see below) is normally distributed around a theoretical PSD $S_x(f)$.

The vector x_r represents the data sampling of the phase fluctuation noise function $x(t)$.

This is a generalization of the TK algorithm described in J. Timmer & M. Konig (1995) developed for single-slope PSDs.

We adopt the following definitions of inverse DFT/DFT:

$$\begin{aligned} X_s &= \sum_{r=1}^{N} x_r e^{-2\pi i(r-1)(s-1)/N};\\ x_r &= \frac{1}{N}\sum_{s=1}^{N} X_s e^{2\pi i(r-1)(s-1)/N}. \end{aligned} \tag{A.10}$$

We generate a set of $N/2+1$ complex numbers

$$X_s = \frac{1}{2}\sqrt{\frac{(N-1)S_x(\nu_s)}{\Delta t}}\left[N_R^s(0,\,1) + i\quad N_I^s(0,\,1)\right];\ s = 1,\ldots,N/2+1, \tag{A.11}$$

where $N_R^s(0,1)$, $N_I^s(0,1)$ are random numbers normally distributed with zero mean and unitary standard deviation (STDEV). It can be easily shown that vector X_s has the following property:

$$<X_s^* X_s> \geqslant \frac{N-1}{2\Delta t} S_x(\nu_s);\ s = 1,\ldots,N/2+1. \tag{A.12}$$

We impose that X_1 and $X_{N/2+1}$ are real, and we extend the X_s to the range $s = N/2+2,\ldots,N$ as

$$X_{N-s+2} = X_s^*;\ s = 2,\ldots,N/2. \tag{A.13}$$

Finally, the simulated phase measurement vector is given by $x_r = \mathrm{IDFT}(X_s)$.

We define a vector of $N/2+1$ frequencies between $\nu_{\rm inf}$ and $\nu_{\rm sup}$,

$$\nu_s = \nu_{\rm inf} + \frac{\nu_{\rm sup} - \nu_{\rm inf}}{N/2}(s-1);\ s = 1,\ldots,N/2+1, \tag{A.14}$$

where $\nu_{\rm inf} = 1/(N-1)/\Delta t$ and $\nu_{\rm sup} = 1/(2\Delta t)$. We assume $\nu_{\rm inf} \neq 0$, as the power-law PSD at zero frequency is not defined if $\alpha < 0$. For the Shannon–Nyquist theorem, the adopted data sampling is equivalent to assuming a null PSD for $\nu > \nu_{\rm sup}$.

For each noise generation, the values of the periodogram

$$P_s = \frac{2\Delta t}{N-1} X_s^* X_s;\qquad s = 1,\ldots,N/2+1 \tag{A.15}$$

will be scattered around $S_x(\nu_s) \pm S_x(\nu_s)$ (i.e., the STDEV coincides with the mean).

A.2. Autocovariance Function and Covariance Matrix

Defining the $2N$-vector

$$x_r' = \{x_r,\,x_r\} = \{x_1,\ldots,x_N,\,x_1,\ldots x_N\}, \tag{A.16}$$

the discrete version of the Wiener–Khinchin theorem reads

$$\begin{aligned} \sum_{r=1}^{N} x_r' x_{r+j-1}' &= \mathrm{IDFT}\left[X_s X_s^\star\right]\\ &= \frac{1}{N}\sum_{s=1}^{N} X_s X_s^\star e^{2\pi i(s-1)(j-1)/N};\quad j = 1,\ldots,N. \end{aligned} \tag{A.17}$$

For a given set of data x_r, we define the (power) autocovariance function as

$$R_x(j-1) = \frac{1}{N-1}\sum_{r=1}^{N}(x_r - \bar{x})(x_{r+j-1} - \bar{x});\quad j = 1,\ldots,N/2+1 \tag{A.18}$$

(since x_r data are real, terms with $j > N/2+1$ are redundant).

Using Equation (A.17), after some algebra, we find

$$\begin{aligned} R_x(j-1) = \frac{2}{N(N-1)}\{&\sum_{s=2}^{N/2} X_s X_s^\star \cos\left[2\pi\frac{(s-1)(j-1)}{N}\right]\\ &+ (-1)^{j-1}\frac{X_{N/2+1}^\star X_{N/2+1}}{2}\};\ j = N/2+1. \end{aligned} \tag{A.19}$$

Since

$$\frac{X_{N/2+1}^\star X_{N/2+1}}{2} = \frac{(x_1 - x_2 + x_3 - \ldots - x_N)^2}{2} \tag{A.20}$$

this term can be safely neglected for large .

By taking the average of Equation (A.19) over a large number of datasets x_r, one obtains (for simplicity we maintain the same notation R_x)

$$\begin{aligned} R_x(j-1) \approx \frac{2}{N(N-1)}\sum_{s=2}^{N/2} <X_s X_s^\star> \cos\left[2\pi\frac{(s-1)(j-1)}{N}\right];\\ j = 1,\ldots,N/2+1. \end{aligned} \tag{A.21}$$

We introduce here $y_1(i,m)$ as a cyclic finite-difference vector with step (i.e., integration time) $\tau = m\Delta t$ to simulate the Doppler data,

$$y_1(i,m) = \frac{x_{i+m} - x_i}{\tau};\quad i = 1,\ldots,N, \tag{A.22}$$

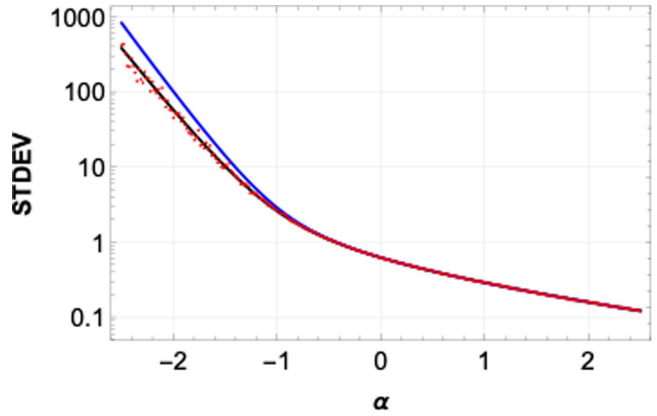


Figure 13. Expected STDEV of simulated y_1 data calculated by using the discrete formula (Equation (A.26); black line) and the continuous formula (Equation (A.8); blue line, with cutoffs) as functions of α. We assumed $h_y = 1$, $N = 10^5$, $\Delta t = 1$ s, and $\tau = \Delta t$. Red points represent the STDEVs of the simulated Doppler data y_1 for several values of α.

and it can be easily shown that

$$Y_{1,s}Y_{1,s}^{\star} = \frac{4}{\tau^2}X_sX_s^{\star}\sin^2\left[\frac{\pi(s-1)\tau}{N\Delta t}\right]. \quad \text{(A.23)}$$

The function $R_{y,1}(j-1)$ can be obtained by Equation (A.21) with $Y_{1,s}Y_{1,s}^{\star}$ instead of $X_sX_s^{\star}$, where $Y_{1,s}Y_{1,s}^{\star}$ is given by Equation (A.23). By substituting, we obtain

$$R_{y,1}(j-1) = \frac{8}{N(N-1)\tau^2}\sum_{s=2}^{N/2} < X_sX_s^{\star} > \sin^2\left[\frac{\pi(s-1)\tau}{N\Delta t}\right] \cos\left[2\pi\frac{(s-1)(j-1)}{N}\right]; j = 1,\ldots,N/2+1. \quad \text{(A.24)}$$

Inserting Equation (A.12) into Equation (A.24), the expected autocovariance function of $y_1(i, m)$ is

$$R_{y,1}((j-1)\Delta t, \tau) = \frac{4}{N\tau^2\Delta t}\sum_{s=2}^{N/2} S_x(\nu_s)\sin^2\left[\frac{\pi(s-1)\tau}{N\Delta t}\right] \cos\left[2\frac{\pi(s-1)(j-1)}{N}\right]; j = 1,\ldots,N/2+1. \quad \text{(A.25)}$$

In the single-slope case, $S_x(f) = h_y/(2\pi)^2 f^{\alpha-2}$,

$$R_{y,1}((j-1)\Delta t, \tau) = \frac{h_y}{N(\pi\tau)^2\Delta t}\sum_{s=2}^{N/2}\nu_s^{\alpha-2}\sin^2\left[\frac{\pi(s-1)\tau}{N\Delta t}\right] \cos\left[2\frac{\pi(s-1)(j-1)}{N}\right]; j = 1,\ldots,N/2+1. \quad \text{(A.26)}$$

That represents the "discrete version" of Equation (A.7). The case $j = 1$ gives the expected variance of y_1.

The Allan variance of y_1 is the variance of

$$y_2(i, m) = \frac{y_1(i, i+m) - y_1(i, m)}{\sqrt{2}}; \quad i = 1,\ldots,N \quad \text{(A.27)}$$

since

$$Y_{2,s}Y_{2,s}^{\star} = 2 \quad Y_{1,s}Y_{1,s}^{\star}\sin^2\left[\frac{\pi(s-1)\tau}{N\Delta t}\right]. \quad \text{(A.28)}$$

We find

$$\sigma_y^2 = \mathrm{AVAR}(y_1) = VAR(y_2) = \frac{2}{N\Delta t}\sum_{s=2}^{N/2}\frac{S_y(\nu_s)}{(\pi\tau\nu_s)^2}\sin^4\left[\frac{\pi(s-1)\tau}{N\Delta t}\right], \quad \text{(A.29)}$$

which represents the "discrete version" of Equation (5).

Equations (A.25) and (A.29) are the expected autocovariance function and the AVAR of a set of data y_1 that fulfill the input PSD of the phase, $S_x(f)$, and of the Doppler noise, $S_y(f)$.

Finally, the expected covariance matrix

$$R_{pq} = R_{y,1}[(i-j)\tau, \tau] \quad p, q = 1,\ldots,N/2+1 \quad \text{(A.30)}$$

can be used as a whitening filter for any colored noise dataset $y_1(i, \tau/\Delta t)$ composed by $N/2+1$ elements.

A.3. Comparison with the Continuous Case

To do a comparison between the "discrete" (Equation (A.26)) and "continuous" (Equation (A.8)) formulae, we assume $S_y(f) = h_y f^{\alpha}$, $h_y = 1$, $N = 10^5$, $\Delta t = 1$ s, $\tau = \Delta t$, $z_{\mathrm{inf}} = \pi\tau/T$, and $z_{\mathrm{sup}} = \pi\tau/(2\Delta t)$, and we limit to the case $j = 0$ (i.e., the variance).

In Figure 13 we report the expected STDEVs of Doppler data y_1 calculated with Equation (A.8) (blue line) and Equation (A.26) (black line), as functions of α. We also report the STDEVs of several sets of simulated Doppler data y_1 obtained with the TK algorithm (red points).

The red points are scattered around the line relative to the discrete formula, while the line relative to the continuous formula tends to overestimate the STDEV for negative values of α (i.e., "red" noise). The scattering of the points is proportional to their expected STDEV; this is a consequence of the fact that the periodograms (Equation (A.15)) of the simulated data have STDEVs equal to the PSDs.

We conclude that, if the noise is generated by the TK algorithm, Equation (A.26) represents the most direct way to obtain the expected autocovariance function.

Appendix B

To infer the spectral slope of the Doppler tropospheric noise component, we considered a set of measured ADEVs for the Cassini mission (L. Iess et al. 2014) at different timescales (τ = 100, 300, and 1000 s). These values were sampled at various percentile levels. A given percentile represents the fraction of observations for which the ADEV is less than or equal to that value (e.g., the 60th percentile corresponds to the ADEV value below which 60% of the data falls).

Given the ADEVs (at different percentage values) at 100, 300, and 1000 s, we rescaled the last two samples to 100 s using the formula

$$\mathrm{ADEV}(\text{rescaled to 100 s}) = \mathrm{ADEV}(@\tau)\left(\frac{\tau}{100}\right)^q, \quad \text{(B.1)}$$

and we estimated the coefficient q in order to have the minimum spread of the data. For winter/summer data we found $q = -0.62$ and -0.44, respectively. Plots are reported in Figure 14. These values of q are compatible with a white noise; therefore, we assume $q = -\frac{1}{2}$.

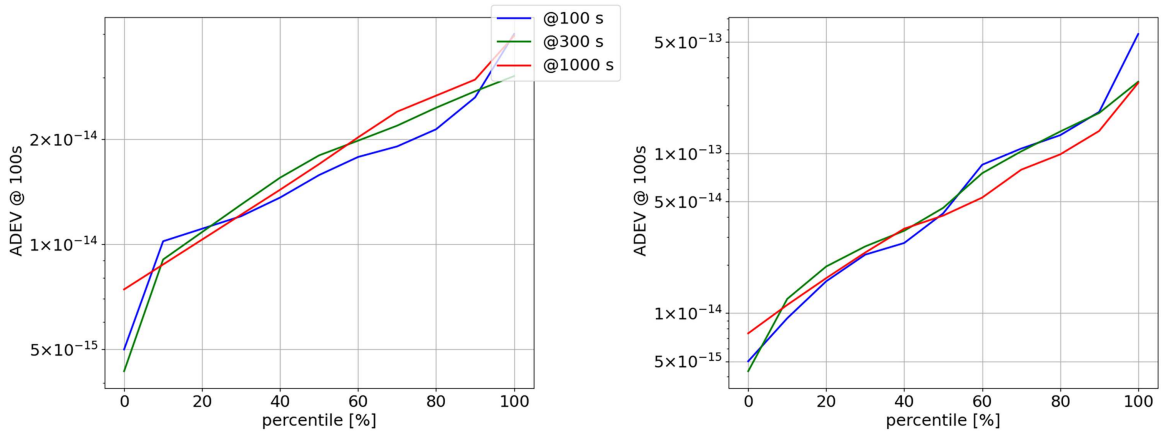


Figure 14. Wet troposphere ADEV (Cassini data). Left: winter. Right: summer. Data correspond to 100 s (blue), 300 s (green), and 1000 s (red) integration time. All data have been rescaled to 100 s by the $(\tau/100)^{-1/2}$.

ORCID iDs

Flavia Giuliani https://orcid.org/0009-0005-9603-3724
Fabrizio De Marchi https://orcid.org/0000-0002-3217-369X
Daniele Durante https://orcid.org/0000-0002-7888-3021
Gael Cascioli https://orcid.org/0000-0001-9070-7947
Luciano Iess https://orcid.org/0000-0002-6230-5825
Erwan Mazarico https://orcid.org/0000-0003-3456-427X

References

Archinal, B. A., Acton, C. H., A'Hearn, M. F., et al. 2018, CeMDA, 130, 22
Asmar, S. W., Armstrong, J. W., Iess, L., & Tortora, P. 2005, RaSc, 40, 1
Bertotti, B., Comoretto, G., & Iess, L. 1993, A&A, 269, 608
Bierman, G. J. 1977, Factorization Methods for Discrete Sequential Estimation, Vol. 128 (1st ed.; Academic)
Buccino, D. R., Kahan, D. S., Parisi, M., et al. 2021, RaSc, 56, e07387
Cascioli, G., Hensley, S., De Marchi, F., et al. 2021, PSJ, 2, 220
Cascioli, G., Mazarico, E., Dombard, A. J., & Nimmo, F. 2024, PSJ, 5, 45
Cascioli, G., Renaud, J. P., Mazarico, E., et al. 2023, PSJ, 4, 65
De Marchi, F., Plumaris, M. K., Burt, E. A., & Iess, L. 2024, ITUFF, 71, 506
Durante, D., Hemingway, D. J., Racioppa, P., Iess, L., & Stevenson, D. J. 2019, Icar, 326, 123
Durante, D., Parisi, M., Serra, D., et al. 2020, GeoRL, 47, e86572
Evans, S., Taber, W., Drain, T., et al. 2018, CEAS, 10, 79
Gargiulo, A. M., Genova, A., Petricca, F., et al. 2024, AcAau, 215, 725
Genova, A., Goossens, S., Lemoine, F. G., et al. 2016, Icar, 272, 228
Giuliani, F., Durante, D., Cascioli, G., et al. 2025, PSJ, 6, 11
Helbert, J., Säuberlich, T., Dyar, M. D., et al. 2020, SPIE, 11502, 1150208
Hensley, S., Smrekar, S., Perkovic-Martin, D., Campbell, B., & Mastrogiuseppe, M. 2020, EPSC, 14, 513
Iess, L., Bertotti, B., & Dobrowolny, M. 1983, A&A, 121, 203
Iess, L., Di Benedetto, M., James, N., et al. 2014, AcAau, 94, 699
Iess, L., Folkner, W. M., Durante, D., et al. 2018, Natur, 555, 220
Iess, L., Rappaport, N. J., Jacobson, R. A., et al. 2010, Sci, 327, 1367
Jacobson, R. A. 2014, AJ, 148, 76
Jacobson, R. A. 2022, AJ, 164, 199
Jones, D. R., Goodson, T., Valerino, P., & Williams, J. 2016, Solar Probe Plus: Unique Navigation Modeling Challenges, in AIAA/AAS Astrodynamics Specialist Conf.
Justh, H., Justus, C. G., & Keller, V. 2006, Global Reference Atmospheric Models, Including Thermospheres, for Mars, Venus and Earth, in AIAA/AAS Astrodynamics Specialist Conf. Exhibit (American Institute of Aeronautics and Astronautics)
Kaula, W. M. 1966, Theory of Satellite Geodesy: Applications of Satellites to Geodesy (Blaisdell)
Keihm, S. J., Tanner, A., & Rosenberger, H. 2004, Measurements and Calibration of Tropospheric Delay at Goldstone from the Cassini Media Calibration System 42–158, Jet Propulsion Laboratory https://ipnpr.jpl.nasa.gov/progress_report/42-158/158A.pdf
Konopliv, A. S., Banerdt, W. B., & Sjogren, W. L. 1999, Icar, 139, 3
Konopliv, A. S., Park, R. S., & Ermakov, A. I. 2020, Icar, 335, 113386
Konopliv, A. S., & Yoder, C. F. 1996, GeoRL, 23, 1857
Kuchynka, P., Folkner, W. M., Konopliv, A. S., et al. 2014, Icar, 229 340
Mackenzie, R., & Folkner, W. M. 2006, Applying Appropriate Weights to Doppler Data, Interoffice Memorandum 343J-06-034, Jet Propulsion Laboratory
Mackenzie, R. A., Iess, L., Tortora, P., & Rappaport, N. J. 2008, GeoRL, 35, L05204
Margot, J. L., Campbell, D. B., Giorgini, J. D., et al. 2021, NatAs, 5, 676
Mariotti, G., & Tortora, P. 2013, RaSc, 48, 111
Marty, J. C., Loyer, S., Perosanz, F., et al. 2011, in 3rd Int. Coll. Scientific and Fundamental Aspects of the Galileo Programme, ESA Proc. WPP326 https://ids-doris.org/images/documents/report/publications/GINS_GRGSsoftware-Marty-2011.pdf
Milani, A., & Gronchi, G. 2009, Theory of Orbit Determination (Cambridge Univ. Press)
Moyer, T. D. 2003, Formulation for Observed and Computed Values of Deep Space Network Data Types for Navigation (Wiley)
Nicholas, J. B., Rowlands, D. D., Luthcke, S. B., et al., 2025 The GEODYN Precision Orbit Determination Software, ESS Open Archive, doi:10.22541/essoar.174051780.04684918/v1
Park, R. S., Mastrodemos, N., Jacobson, R. A., et al. 2024, JGRE, 129, e2023JE008054
Smrekar, S., Hensley, S., Nybakken, R., et al. 2022, in 2022 IEEE Aerospace Conf. (AERO) (Big Sky, MT, USA: IEEE), 1
Tapley, B. D., Schutz, B. E., & Born, G. H. 2004, Statistical Orbit Determination (Elsevier)
Thornton, C. L., & Border, J. S. 2003, Radiometric Tracking Techniques for Deep-Space Navigation (Wiley-Interscience) https://descanso.jpl.nasa.gov/monograph/series1/Descanso1_all.pdf
Timmer, J., & Konig, M. 1995, A&A, 300, 707
Wallace, M. S., Sweetser, T. H., Haw, R. J., Lau, E., & Hensley, S. 2019, in 29th AAS/AIAA Space Flight Mechanics Meeting
Walls, F. L., & Allan, D. W. 1986, IEEEP, 74, 162
Wieczorek, M. A. 2015, Treatise on Geophysics (Elsevier), 153